1   **Transient non-specific DNA binding dominates the target search of bacterial DNA-binding**
2   **proteins**

3

4   Mathew Stracy*[a], Jakob Schweizer[b], David J Sherratt[a], Achillefs N Kapanidis[c], Stephan Uphoff*[a],
5   Christian Lesterlin*[d]

6   [a]Department of Biochemistry, University of Oxford, Oxford OX1 3QU, United Kingdom

7   [b]Max Planck Institute for Dynamics of Complex Technical Systems, Magdeburg

8   [c]Biological Physics Research Group, Clarendon Laboratory, Department of Physics, University of
9   Oxford, Oxford OX1 3PU, United Kingdom

10   [d]Molecular Microbiology and Structural Biochemistry (MMSB), Université Lyon 1, CNRS, Inserm,
11   UMR5086, 69007, Lyon, France
12

13   *Correspondence to: mathew.stracy@bioch.ox.ac.uk; stephan.uphoff@bioch.ox.ac.uk

14   christian.lesterlin@ibcp.fr

15   **ABSTRACT**

16   **Despite their diverse biochemical characteristics and functions, all DNA-binding proteins share**

17   **the ability to accurately locate their target sites among the vast excess of non-target DNA.**

18   **Towards identifying universal mechanisms of the target search, we used single-molecule tracking**

19   **of 11 diverse DNA-binding proteins in living *Escherichia coli*. The mobility of these proteins**

20   **during the target search was dictated by DNA interactions, rather than by their molecular**

21   **weights. By generating cells devoid of all chromosomal DNA, we discovered that the nucleoid does**

22   **not pose a physical barrier for protein diffusion, but significantly slows the motion of DNA-**

23   **binding proteins through frequent short-lived DNA interactions. The representative DNA-**

24   **binding proteins (irrespective of their size, concentration, or function) spend the majority (58-**

25   **99%) of their search time bound to DNA and occupy as much as ~30% of the chromosomal DNA**

26   **at any time. Chromosome-crowding likely has important implications for the function of all DNA-**

27   **binding proteins.**

28

29   **INTRODUCTION**

30   DNA is organized into chromosomes that must be maintained in a highly compacted state, while

31   keeping the genetic information accessible for processing by many DNA-binding proteins. The ability

32   of these proteins to identify and bind to specific DNA target sites among the vast excess of non-target

33   DNA is crucial to fundamental cellular functions, including the recruitment of transcription factors to

34   promoter sequences, of DNA repair proteins to DNA lesions, or of DNA topoisomerases to supercoiled

35   DNA strands, to name just a few. In all organisms, diffusion is the primary mechanism by which DNA-

36   binding proteins locate their target sites on chromosomes (Erbaş and Marko, 2019; Erbaş et al., 2019;

37   Schavemaker et al., 2018). The diffusion coefficient of a particle in a dilute solution is determined by

38   its size, as well as the viscosity and temperature of the medium. Within the crowded and heterogeneous

39   intracellular environment, however, a myriad of specific and non-specific interactions as well as steric

40   effects influence the mobility of macromolecules. Because of this complexity, efforts to understand

41   molecular mobility have relied on phenomenological models (Kalwarczyk et al., 2012; Mika and

42   Poolman, 2011) or coarse-grained simulations of the cytoplasm (Chow and Skolnick, 2017; Feig et al.,

43   2015; Hasnain et al., 2014). In this context, analysis of *in vivo* experimental data is crucial not only to

44   determine parameter values but also the structure of such models by informing which cellular

45   components and interactions should be included in a model.

46

47   Contrary to eukaryotes, bacterial chromosomes are not compartmentalized into a nucleus, but organized

48   into nucleoid structures without a physical barrier from the cytoplasm. The 4.6 Mbp *E. coli* chromosome

49   with a contour length of 1.6 mm is compacted into a volume of ~1 μm^3 via DNA supercoiling, entropic

50   forces, as well as protein-DNA and RNA-DNA interactions, and occupies ~60% of the bacterial cell

51   volume (Gray et al., 2019). Outside the nucleoid, the cytoplasm is mainly comprised of RNA and

52   proteins. A longstanding question is whether the presence of the dense nucleoid mesh affects the

53   mobility of all cytoplasmic proteins, regardless of their ability to bind DNA. The chromosome could

54   pose a steric barrier, resulting in confined diffusion, and preventing larger proteins from accessing the

55   densest regions of the nucleoid (Kalwarczyk et al., 2012; Konopka et al., 2006; Kuznetsova et al., 2014).

56   Furthermore, the target-search process is subject to a trade-off between speed and accuracy to

57   distinguish target from non-target sites (Zandarashvili et al., 2015). Accumulating experimental

58   evidence supports theoretical considerations that the search efficiency is maximized by "facilitated

59   diffusion", which is the combination of 3D protein diffusion with non-specific binding and 1D sliding

60   along DNA (Halford and Marko, 2004; Hammar et al., 2012; Hippel and Berg, 1989). Together with

61   chromosome crowding effects, the relative contribution of 3D and 1D diffusion modes during the target

62   search should strongly affect the overall mobility of DNA-binding proteins *in vivo*.

63

64 Fluorescence microscopy-based methods such as Fluorescence Correlation Spectroscopy (FCS) (Bacia
65 et al., 2006; Cluzel et al., 2000) and Fluorescence Recovery After Photobleaching (FRAP) (Konopka
66 et al., 2006; Kumar et al., 2010; Mika and Poolman, 2011; Mika et al., 2010; Mullineaux et al., 2006;
67 Nenninger et al., 2010; Ramadurai et al., 2009) have been used to investigate protein mobility in live
68 bacterial cells. More recently, it has become possible to directly visualize aspects of the target search
69 of individual proteins in live cells using single-molecule microscopy (Elf et al., 2007; Hammar et al.,
70 2012; Kapanidis et al., 2018; Normanno et al., 2015; Rhodes et al., 2017). These studies focused on a
71 limited number of test proteins, typically the Lac repressor or other transcription factors, raising the
72 question whether the proposed models for the target search are universal for diverse types of DNA-
73 binding proteins. Although the observed intracellular mobility and spatial distribution of DNA-binding
74 proteins suggest that non-specific DNA interactions play an important role in their target search
75 kinetics, these interactions appeared too transient for direct visualization and quantification by live-cell
76 imaging (Garza de Leon et al., 2017; Stracy et al., 2015, 2016; Uphoff et al., 2013). In previous attempts
77 to resolve this issue, the DNA-binding affinity of the protein studied was perturbed genetically (Elf et
78 al., 2007), but for some proteins this approach is not readily tractable. Alternatively, protein mobility
79 has been compared between different regions of the cell with lower or higher DNA density (Bakshi et
80 al., 2011; Sanamrad et al., 2014; Stracy et al., 2015). However, since few DNA-binding proteins are
81 located in DNA-free regions of the cell, it is difficult to accurately measure their diffusion with this
82 approach. Furthermore, even with super-resolution microscopy, the exact shape and boundary of the
83 nucleoid are not well defined (Le Gall et al., 2017; Stracy et al., 2015).

84

85 To overcome this uncertainty and to determine the influence of the nucleoid DNA on protein mobility,
86 we measured the mobility of DNA-binding proteins in cells devoid of chromosomal DNA. To this end,
87 we developed a method to remove all chromosomal DNA from cells. By comparing protein diffusion
88 in DNA-free cells and unperturbed cells, we identified universal features of the target search process
89 for 11 DNA-binding proteins with a broad range of sizes, biochemical characteristics and functions.
90 This, combined with diffusion simulations, allowed us to quantitatively partition the behavior of diverse
91 DNA-binding proteins into long-lived DNA-binding at target sites, transient non-specific DNA-
92 binding, and free diffusion between DNA strands. We found that the intracellular mobility of proteins
93 during their target search is primarily dictated by transient interactions with the DNA, rather than by
94 their molecular weight or intracellular concentration. The representative DNA-binding proteins
95 (irrespective of their size, concentration, or function) spend the majority (58-99%) of their search time
96 bound to DNA, occupying as much as ~30% of the chromosomal DNA at any time.

97

98 **RESULTS**

Live-cell single-molecule tracking of a variety of DNA-binding proteins

To uncover universal mechanisms that govern the target search process of DNA-binding proteins in general, we measured the diffusion characteristics of 11 different proteins involved in various types of DNA transactions and spanning a large range of molecular weights and concentrations inside the cell. These included proteins whose target is a specific DNA sequence such as RNA polymerase (β' subunit, RpoC), the low copy number transcription factor LacI, and the abundant histone-like nucleoid-associated proteins HU and H-NS. We further analyzed proteins which target DNA structural motifs such as DNA topoisomerases (ParC, GyrA) which act on supercoiled DNA, or DNA polymerase I (Pol1) and DNA ligase (LigA) which recognize gapped or nicked DNA respectively. Lastly, we also studied DNA-repair proteins which recognize DNA lesions (UvrA) or mismatches (MutS), and the Structural Maintenance of Chromosomes (SMC) protein MukB which is involved in chromosome organization but binds DNA with little known specificity.

To examine the mobility of this diverse set of proteins, we use single-molecule tracking, a method that provides a direct readout of protein mobility inside living cells (Gahlmann and Moerner, 2014; Li et al., 2018; Uphoff and Sherratt, 2017). We imaged proteins that were fused to the photoactivatable fluorescent protein PAmCherry (Subach et al., 2009), and expressed from their endogenous chromosome locus in *Escherichia coli* cells. The use of a photoactivatable fluorophore allows tracking proteins at their native expression levels by imaging single molecules, one at a time, while the rest of the molecules reside in a non-fluorescent state (Bakshi et al., 2011; English et al., 2011; Manley et al., 2008; Niu and Yu, 2008; Uphoff et al., 2013). We recorded movies on a custom-built microscope using near-Total Internal Reflection Illumination (Tokunaga et al., 2008; Wegel et al., 2016) with sparse photoactivation at a frame rate of 15 ms/frame for >5000 frames to resolve the motion of hundreds of molecules per cell in multiple cells per field of view. Following automated localization and particle tracking analysis, the apparent diffusion coefficient D* was calculated from the mean-squared displacement (MSD) of each trajectory (Uphoff, 2016) (Fig. 1A).

Computing D* from particle-tracking data tends to underestimate the actual diffusion coefficient D for molecules with high mobility because of measurement biases, including the blurring of fluorescent spots due to molecular motion during the camera exposure and the confinement of trajectories within the cell volume (Uphoff, 2016). Hence, we initially analyzed apparent diffusion coefficients and subsequently employed diffusion simulations to correct the biases (see below). Molecular subpopulations that differ in mobility can be detected as separate species in D* distributions. In particular, proteins that remain bound to DNA over the entire trajectory appear essentially immobile due to the slow and constrained motion of chromosomal DNA (Elmore et al., 2005).

The mobility of DNA-binding proteins is independent to their molecular weights.

136   The average intracellular mobility of the different DNA-binding proteins varied strongly, ranging from
137   mostly immobile proteins such as HNS (mean $D^* = 0.17$ μm^2/s) to mostly diffusing proteins such as
138   LigA (mean $D^* = 1.14$ μm^2/s) (Fig. 1B). There was no obvious relation between the observed mobility
139   and the type of DNA interactions (e.g. sequence-specific, structure-specific, or lesion binding). To
140   distinguish between proteins specifically bound to DNA and mobile proteins searching for target sites
141   we first determined the apparent mobility of proteins specifically bound to DNA by measuring the
142   motion of Pol1 molecules recruited to DNA damage sites generated by treating cells with the DNA-
143   alkylating agent methyl methanesulfonate (MMS, 100 mM) (Fig. S1A), which resulted in an increase
144   in molecules which are immobile (with $D_{imm}^*=0.11$ μm^2/s) for the entire trajectory (5 frames, 75 ms),
145   as previously observed (Uphoff et al., 2013). For other proteins in this study we have previously
146   observed a similar increase in 'long-lived' immobile molecules ($D_{imm}^*=0.11$ μm^2/s) upon recruitment
147   to specific target sites after induction of DNA damage (LigA, UvrA, MutS; Stracy et al., 2016; Uphoff
148   et al., 2013, 2016), or by capturing DNA-bound enzymes during catalysis by drug treatment (GyrA,
149   ParC; Stracy et al., 2019; Zawadzki et al., 2015). We previously observed a decrease in the long-lived
150   immobile population of RNAP upon addition of a transcription-inhibiting drug (Stracy et al., 2015),
151   and a similar decrease for LacI after removing its chromosomal binding site (Garza de Leon et al.,
152   2017). Together, these studies show that the long-lived immobile population represents proteins
153   specifically bound at DNA target sites. The apparent mobility of these DNA-bound molecules was
154   slightly above the localization uncertainty of $\sigma= 35$ nm measured in chemically fixed cells (giving an
155   apparent $D_{fixed}^*=0.07$ μm^2/s; Fig. S1B). By subtracting the contribution of the localization uncertainty
156   to the observed D^* (Michalet and Berglund, 2012), we estimate the mobility of proteins bound to DNA
157   loci for the entire trajectory as $D^*_{bound} = 0.04$ μm^2/s.

158

159   To determine the relative abundances and average diffusion coefficients of mobile molecules searching
160   for target sites and long-lived immobile molecules bound to DNA, we fitted the D^* histograms using
161   an analytical function derived from a two-species Brownian motion model (Stracy et al., 2015) (Fig.
162   1B and S1A-B). The quantification confirmed our initial observations that the different DNA-binding
163   proteins exhibit vastly different mobility inside cells, both in terms of the fraction of mobile and
164   immobile molecules (ranging from 96 % of mobile for Pol1 to 23 % mobile for H-NS molecules) (Fig.
165   1C), and in terms of the diffusion coefficients of the mobile molecules (ranging from 0.33 μm^2/s for
166   HU to 1.2 μm^2/s for LigA) (Fig. 1D).

167

168   According to the Stokes-Einstein equation for Brownian motion, the diffusion coefficient of a spherical
169   particle is related to its mass: $D \sim M^{-1/3}$. To test this relation for the DNA-binding proteins, we plotted
170   D^* of molecules in the mobile state against the known molecular weights of each protein (Fig. 1E).
171   Strikingly, the *in vivo* mobility of DNA-binding proteins was largely independent of their mass.
172   Although non-spherical proteins are expected to deviate from the Stokes-Einstein law, this does not

173   explain the absence of any correlation between mass and mobility. In contrast, previous studies showed

174   a clear dependence of mass on the mobility of cytoplasmic proteins with no affinity for DNA

175   (Kalwarczyk et al., 2012; Kumar et al., 2010; Nenninger et al., 2010). Our results indicate that the

176   apparent mobility of DNA-binding proteins is dictated by molecular interactions independent of protein

177   mass. There was also no trend between the mobility and the intracellular concentration of the different

178   proteins (Fig. S1C).

179

180   **DNA-binding proteins remain closely associated with the nucleoid during their target search.**

181   We examined the spatial distribution of mobile DNA-binding proteins relative to the nucleoid. As an

182   example, we tracked Pol1-PAmCherry and RNAP-PAmCherry in live cells that were stained with

183   SytoGreen dye to label DNA (Fig. 2A-B). The spatial distributions of mobile molecules closely

184   overlapped with the nucleoid. Similarly, when averaged over many cells and the intracellular position

185   of the mobile population of molecules clearly demarcates the nucleoid shape (Fig. 2D). This was in

186   contrast to ribosomal protein S1, which has no direct DNA affinity. Consistent with previous reports

187   (Sanamrad et al., 2014), the slow-moving S1 molecules, which are presumably incorporated into

188   ribosomes, resided outside the nucleoid area, whereas the mobile unincorporated subunits are uniformly

189   distributed throughout the cell (Fig. 2C-D). We hypothesized that the enrichment of mobile DNA-

190   binding proteins within the nucleoid is caused by transient interactions with DNA during the target

191   search process. The computation of D* values is based on the average movement of a molecule over a

192   series of frames (here 5 frames, 75 ms). The observed mobility thus reflects a time-average of the

193   diffusion coefficient where 3D diffusion is interrupted by multiple transient binding events with a

194   duration below 75 ms. Consistent with this view, we observed that the mobility of DNA-binding

195   proteins increased and tracks spread throughout the cell cytoplasm after treatment with the antibiotic

196   rifampicin, which causes decompaction of the nucleoid (Fig. S1D) (Cabrera et al., 2009; Dworsky and

197   Schaechter, 1973; Stracy et al., 2015).

198

199   **Generating chromosome-free cells to study protein diffusion in the absence of DNA**

200   The association of mobile DNA-binding proteins with the nucleoid could reflect a genuine DNA-

201   binding activity or be the result of a sieving effect where protein movement is slowed within the

202   nucleoid by physical entrapment within the mesh of DNA strands. To distinguish between the effects

203   of sieving and non-specific DNA interactions, we devised a method that eliminates protein-DNA

204   interactions entirely by removing all chromosomal DNA from cells, while retaining the same cell size

205   and intracellular protein concentration. To this end, we used the I-SceI restriction endonuclease from

206   *Saccharomyces cerevisiae* (Monteilhet et al., 1990), which introduces site-specific double-stranded

207   DNA breaks (DSBs) at *I-SceI* cut sites (*I-SceI^cs*) inserted into the *E. coli* chromosome (Fig. 3A)

208   (Lesterlin et al., 2013; Meddows et al., 2004). In the absence of RecA, which is essential for
209   homologous recombination, creation of DSBs by I-SceI results in complete degradation of the
210   chromosome by the RecBCD helicase-nuclease complex, a phenomenon referred to as *reckless*
211   chromosome degradation (Skarstad and Boye, 1993; Willetts and Clark, 1969). To minimize the time
212   required for complete chromosome degradation, we inserted two cut sites diametrically opposed on the
213   genetic map of the chromosome: in the *ilvA* locus (3953 kb) close to the origin of replication, and in the
214   *ydeO* locus (1580 kb) in the *terminus* region (referred to as OT strain) (Fig. 3A). We then inactivated
215   the *recA* gene by mutation in these strains carrying *Origin-Terminus* cut sites (referred to as OT*recA-*).
216   Chromosome degradation was triggered by the expression of the plasmid-borne *I-SceI* gene under the
217   control of an arabinose-inducible promoter. Chromosome degradation after *I-SceI* induction resulted in
218   the progressive disappearance of DAPI-stained DNA from cells (Fig. 3B), which was complete within
219   120 to 160 min in most (~92%) cells (Fig. 3C, Fig. S2A-B). This reflects the time required for 4
220   RecBCD complexes to each degrade approximately one quarter of the chromosome (~1150 kb) from
221   the 4 DNA ends generated by 2 DSBs at a speed of ~160 bp per second, consistent with previous results
222   (Lesterlin et al., 2014). Before arabinose induction, a fraction of cells (~17%) already exhibited DNA
223   degradation due to leaky I-SceI expression (Fig. S2A-B). We also found that a fraction (~8 %) of cells
224   did not exhibit complete chromosome loss after 120 min (Fig. S2A-B), likely due to heterogeneous
225   induction of I-SceI from the arabinose-inducible promoter in the cell population (Siegele and Hu, 1997)
226   or because of the limiting number of RecBCD molecules per cell (Lepore et al., 2019). In the following,
227   to ensure our results reflected completely chromosome-free cells, we excluded cells that showed any
228   remaining fluorescent DNA stain from our analysis.
229

230   **Chromosome-free cells remain metabolically active for several hours**
231   Since protein mobility is influenced by the metabolic state of the cell (Parry et al., 2014), we explored
232   if cells remained metabolically active after chromosome degradation using two independent assays.
233   First, to test if ATP-driven mechanisms were affected by chromosome loss, we turned to the well-
234   characterized ATP-dependent Min system, whose three components MinCDE are important for
235   defining the position of the division site (Lutkenhaus, 2007). Coupled protein–protein and protein–
236   membrane interactions generate pole-to-pole dynamic oscillation of MinC, which is highly sensitive to
237   ATP concentrations (Hu et al., 2002). These oscillations are particularly striking in cells that have been
238   grown into long filaments by treatment with the antibiotic cephalexin (Raskin and de Boer, 1999). We
239   found that the MinC-Ypet oscillation period was ~17 seconds with a wavelength of ~10 μm, both in
240   unperturbed cells and after chromosome degradation (Fig. 3D-G and Fig. S3), demonstrating that ATP
241   concentration in chromosome-free cells remained stable for at least 2 hours. Our results also indicate
242   that the presence of the nucleoid DNA has no influence on Min protein dynamics, in contrast to a

243   previous report that the oscillations may be coupled to chromosome segregation (Di Ventura et al.,

244   2013).

245

246   Second, to test if protein synthesis activity was maintained after chromosome loss, we used a non-

247   degraded plasmid producing a reporter protein ParB-mCherry from a P_{lac} promoter. We found that

248   IPTG-induced ParB-mCherry production continued for ~200 min after I-SceI induction (Fig. S4A).

249   Together, these tests establish that our chromosome degradation strategy is appropriate to study protein

250   diffusion in metabolically active chromosome-free cells. Furthermore, in order to validate the use of

251   this genetic system, we confirmed that protein diffusion was not affected by inactivation of RecA *per*

252   *se*, or by induction of I-SceI in cells that do not contain any I-SceI cut sites, nor by DSB creation in

253   RecA+ DNA repair-proficient cells (Fig S4B-C).

254

255   **The mobility of the Lac repressor increases in DNA-free cells.**

256   To test the effect of chromosome loss on intracellular diffusion, we first focused on the lac repressor

257   (LacI) as a prototypical DNA-binding protein which searches for operator sequences by facilitated

258   diffusion involving frequent non-specific DNA binding, rotation-coupled sliding and hopping (Elf et

259   al., 2007; Garza de Leon et al., 2017; Hammar et al., 2012; Kao-Huang et al., 1977; Marklund et al.,

260   2020). Chromosome degradation, ~120 min after I-SceI induction, drastically changed the diffusion

261   behavior of LacI-PAmCherry (Fig. 4A). We no longer detected any immobile molecules; further, the

262   mobility of the diffusing population increased significantly (from $D^* = 0.43$ $\mu m^2/s$ in unperturbed cells

263   to $D^* = 1.5$ $\mu m^2/s$ in chromosome-free cells). The change in diffusion pattern is apparent in the D^*

264   distribution (Fig. 4A), MSD curves (Fig. 4B), and cumulative distributions of displacements (Fig. 4C).

265   We identified a subpopulation of cells (~15 %) that exhibited no change in LacI diffusion after I-SceI

266   induction; however, DNA staining prior to single-molecule tracking showed that these cells had no or

267   incomplete chromosome loss and these cells were thus excluded (Fig. S5A-B). The strong influence of

268   the presence of the chromosome on LacI mobility could be due to DNA-binding and sliding, or the

269   result of a general molecular sieving effect, where protein motion is hindered because of entrapment

270   within the chromosome meshwork. The latter effect should influence the motion of all proteins in the

271   cell, even those that have no DNA affinity. To test this directly, we imaged a truncated LacI[-41] mutant

272   with most of its DNA-binding domain (41 amino acids from the N-terminus) removed. For this mutant

273   all specific and non-specific DNA binding modes are abolished (Elf et al., 2007; Garza de Leon et al.,

274   2017), and hence shows essentially no immobile molecules (Fig. 4D). Notably, LacI[-41] also had a much

275   higher apparent diffusion coefficient than the mobile population of wild-type LacI ($D_{lacI-41}^*=1.3$ $\mu m^2/s$

276   vs $D_{lacI}^*=0.43$ $\mu m^2/s$). This difference far exceeded the 2–3% change expected solely from the 9 kDa

277   decrease in the protein size due to the truncation (considering $D \sim M^{-1/3}$). After chromosome

278   degradation, LacI^{-41} only showed a small increase in mobility (from D*=1.3 μm^2/s to 1.5 μm^2/s) (Fig.

279   4B-D). To test if this is general, we also measured the diffusion of unconjugated PAmCherry alone and

280   found no significant change between unperturbed and chromosome-free cells (Fig. 4C). Therefore, the

281   presence of the chromosome has only a minor influence on the diffusion of a protein that has no affinity

282   for DNA. This is consistent with observations that the fluorescent proteins mEOS and Kaede diffuse

283   inside the whole cell volume with no evidence that the presence of the nucleoid hinders their motion

284   (Bakshi et al., 2011; English et al., 2011). Note that these data do not exclude the possibility that DNA

285   sieving may hinder the movement of proteins and macromolecular complexes that are much larger than

286   LacI and fluorescent proteins, such as 70S ribosomes which are occluded from the nucleoid (Fig. 2C,

287   and Sanamrad et al., 2014).

288

Transient DNA interactions strongly affect the mobility of diverse DNA-binding proteins.

290   Having established that chromosome degradation increases the mobility of LacI primarily because of a

291   loss of DNA interactions, we asked if this was generally the case for diverse types of DNA-binding

292   proteins. We chose four proteins representing distinct types of DNA interactions (Fig. 5A): RNA

293   polymerase (RNAP) recognizes specific promoter sequences to initiate RNA synthesis and transcribe

294   genes (Mazumder and Kapanidis JMB 2019); DNA polymerase I (Pol1) recognizes gapped or nicked

295   structures in DNA repair and replication (Joyce and Steitz, 1994); Structural Maintenance of

296   Chromosomes protein MukB interacts non-specifically with double-stranded DNA to aid chromosome

297   segregation (Nolivos et al., 2016; Reyes-Lamothe et al., 2012; Rybenkov et al., 2014); Ligase (LigA)

298   interacts with DNA nicks and catalyzes the joining of DNA ends (Shuman, 2009). These proteins not

299   only have different biological functions, but also differ in their shapes, molecular weights, oligomeric

300   states, and intracellular concentrations. The RNAP holoenzyme with the initiation factor σ^{70} is a 449

301   kDa complex composed of 6 different proteins and present at 3000-6000 copies per cell (Bakshi et al.,

302   2013; Endesfelder et al., 2013; Stracy et al., 2015). Pol1 is a monomeric 104 kDa protein with two

303   globular domains connected by a flexible linker and present at ~500 copies per cell (Uphoff et al., 2013).

304   MukB has a characteristic elongated SMC protein fold with globular domains on either end of 50-nm

305   long coiled-coil domains. Approximately 100 MukB homodimers per cell likely form large 890 kDa

306   complexes with MukE and MukF proteins (Badrinarayanan et al., 2012). Ligase is a monomeric 73 kDa

307   enzyme present at a ~100 copies per cell that encircles the DNA as a C-shaped protein clamp

308   (Nandakumar et al., 2007; Shuman, 2009).

309

310   Considering the differences in the function and physical characteristics of RNAP, Pol1, MukB, and

311   LigA, any shared aspects of their diffusion behavior are likely to indicate universal mechanisms of the

312   DNA target search. In unperturbed cells, a large fraction of RNAP-PAmCherry and MukB-PAmCherry

313   molecules were immobile or slowly diffusing (RNAP: $D^* = 0.36$ µm^2/s, MukB: $D^* = 0.39$ µm^2/s),

314   whereas Pol1-PAmCherry and LigA-PAmCherry molecules were rarely immobile for the entire

315   trajectory and diffused faster ($D^* = 1.0$ µm^2/s and $D^* = 1.2$ µm^2/s respectively) (Fig. 5B), consistent

316   with our previous observations (Badrinarayanan et al., 2012; Stracy et al., 2015; Uphoff et al., 2013).

317   Despite the differences in the diffusion profiles, a unifying feature was the clear nucleoid-association

318   of the tracks for all three proteins in unperturbed cells (Fig. 5B; Fig. 2). Chromosome degradation had

319   the same effects for all four proteins (compare Fig. 5B and C): the populations of long-lived immobile

320   molecules disappeared, and diffusion of the mobile proteins increased substantially (RNAP: $D^* = 1.2$

321   µm^2/s, Pol1: $D^* = 1.9$ µm^2/s, MukB: $D^* = 0.66$ µm^2/s, MukB: $D^* = 1.9$ µm^2/s) (Fig. 5C). Furthermore,

322   the tracks filled the entire cytoplasm of chromosome-free cells (Fig. 5C). These results match our

323   observations for the Lac repressor (Fig. 4), and taken together, they demonstrate that transient DNA

324   interactions dictate the mobility and spatial distribution of diverse types of DNA-binding proteins.

325

The mobility of DNA-binding proteins shows a steep size-dependence in chromosome-free cells

327   Accurate quantification of diffusion coefficients from single-molecule tracking experiments requires

328   consideration of several biases such as localization error and confinement within the cell volume

329   (especially for rapidly moving molecules) (Uphoff, 2016). In order to account for these potential biases

330   to determine accurate D values from experimentally measured D^*, we applied stochastic Brownian

331   motion simulations to generate artificial single-molecule tracks using an identical number of molecules

332   inside the same segmented 3D cell volumes as in the experimental data (Fig. 6A). Localization error

333   and stochastic disappearance of tracks due to photobleaching were also modeled, resulting in the same

334   sampling and biases as in the experimental D^* distributions. We determined an unbiased estimate of

335   the diffusion coefficient D from the best match (according to a least-squares metric) between D^*

336   distributions observed in experiments and those obtained from simulations with a range of input

337   diffusion coefficients.

338   Using this procedure, we estimated the mean unbiased diffusion coefficients of LacI, RNAP, Pol1,

339   LigA, and MukB molecules after chromosome degradation (D_{free} values in Table 1). To verify that these

340   values are robust with regards to the data acquisition and simulation parameters, we also performed

341   single-molecule tracking experiments at three-fold shorter camera exposure times (5 ms) and obtained

342   the same results from the corresponding simulations (Fig. S6). Although there was no correlation

343   between the mass and the diffusion coefficient of DNA-binding proteins in unperturbed cells (D_{mobile}),

344   we found a clear inverse relation in chromosome-free cells (D_{free}) (Fig. 6B). Fitting a power-law $D_{free} =$

345    $c \cdot M^{\alpha}$ yielded an exponent of $\alpha = -0.75$, showing that protein mobility decreases more steeply with

346   increasing mass than predicted by the Stokes-Einstein model ($\alpha = -0.33$). Therefore, the crowded

347   cytoplasm has sieving properties even in the absence of the chromosome meshwork. Indeed, the

348   diffusion of DNA-binding proteins in DNA-free cells shows a similar mass dependence as cytoplasmic

349   proteins that have no DNA-binding function in unperturbed cells (α = -0.7) (Mika and Poolman, 2011).

350

351   **Transient DNA-binding events dominate the target search.**

352   Comparison of the diffusion coefficient in unperturbed cells versus chromosome-free cells allows

353   quantifying the contribution of non-specific DNA interactions to the observed mobility of DNA-binding

354   proteins during the target search. By simulating molecules rapidly interconverting between freely

355   diffusing (with D_{free} determined from chromosome-free cells) and DNA-bound (D_{bound} = 0.04 μm^2/s)

356   we can establish the fraction of time a protein spends transiently bound to DNA, $\Phi_{transient\_binding}$, which

357   best recapitulates the observed mobility of mobile molecules during their target search measured in

358   unperturbed cells (D^*_{mobile}, Fig. 1B). Using this approach we find that $\Phi_{transient\_binding}$ > 0.5 for RNAP,

359   Pol1, MukB, and LigA, demonstrating that they spend the majority of their search process non-

360   specifically bound to DNA ($\Phi_{transient\_binding}$ RNAP: 87%, LacI: 93%, Pol1: 61%, MukB: 58%; LigA:

361   60%) (Fig. 6C). The value for LacI is in good agreement with a previous estimate (Elf et al., 2007).

362   Including the populations of long-lived immobile molecules measured in unperturbed cells

363   (representing molecules likely to be bound at specific DNA target sites, Fig. 1) in the calculations, the

364   total percentage of DNA-bound molecules at any time is even higher (RNAP: 93%, LacI: 96%, Pol1:

365   63%, MukB: 82%; LigA: 63%) (Fig. 6D). Based on these results, we report a quantitative partitioning

366   of DNA-binding proteins into three distinct states of mobility: long-lived specific binding at DNA target

367   sites, transient non-specific DNA-binding, and free diffusion between DNA strands (Fig. 6C-D).

368   Using the estimate of α = -0.75 to extrapolate D_{free} and the measured % of long-lived DNA binding and

369   the measured D^*_{mobile} values, we performed the same partitioning of diffusive states for all the DNA-

370   binding proteins considered in this study (Table 1). In all cases, the fraction of the target search spent

371   non-specifically bound to DNA was >50%, and for the small nucleoid associated protein HU this

372   estimated fraction was as high as 99%.

373

374   **DISCUSSION**

375   Our study demonstrates the ubiquity of transient non-specific DNA interactions for diverse DNA-

376   binding proteins *in vivo*. Despite their different sizes, DNA targets, mobility, and copy numbers in the

377   cell, the target search of all the DNA-binding proteins examined here is dominated by transient non-

378   specific DNA binding. Considering such widespread and frequent non-specific DNA interactions of all

379   types of DNA-binding proteins, an important question is how these in turn affect DNA transactions.

380   Our catalogue of the intracellular mobility of different types of DNA-binding proteins can serve as a

381   general reference and should aid ongoing efforts to generate physical models of the intracellular
382   environment.

383   Our analysis shows that the chromosome DNA mesh does not constitute a physical barrier for the
384   intracellular motion of proteins (at least up to a protein weight of 100 kDa). In fact, mobile DNA-
385   binding proteins (even large complexes such as RNAP) are enriched in the densest regions of the
386   nucleoid by frequent non-specific DNA interactions. These results demonstrate that the apparent
387   mobility of DNA-binding proteins depends on DNA-binding activity rather than molecular weight, as
388   concluded from previous FRAP experiments (Kumar et al., 2010). While we have found no evidence
389   of a nucleoid sieving effect for DNA-binding proteins during their target search, previous reports have
390   established that large macromolecular complexes which do not bind DNA, such as protein aggregates,
391   70S ribosomes, and MS2-RNA systems are excluded from the nucleoid (Landgraf et al., 2012; Lindner
392   et al., 2008; Stracy et al., 2015; Stylianidou et al., 2014). Smaller non-DNA-binding complexes such as
393   individual ribosomal subunits appear to diffuse freely through the nucleoid (Sanamrad et al., 2014).
394   Together, these findings are consistent with the view that DNA-interacting proteins can diffuse freely
395   in the whole cell compartment and are enriched within the nucleoid volume due to frequent non-specific
396   interactions with the DNA. Protein hopping or sliding along the DNA can enhance the search efficiency
397   for any individual protein, while overcrowding the chromosome with non-specifically bound proteins
398   would globally reduce the search kinetics due to the obstruction of target sites and sliding collisions (Li
399   et al., 2009). This trade-off likely influenced the evolution of protein abundances and their non-specific
400   DNA binding affinities.

401   Given the diversity of the proteins we have tested, their target-specific DNA interactions are likely to
402   be very different from each other, suggesting that a more universal interaction plays the largest role in
403   the abundant transient DNA binding during the target search. We speculate that the electrostatic
404   interaction between positively charged functional groups on the surface of the proteins and the largely
405   invariant negatively charged phosphate backbone of the DNA may drive this phenomenon (Kalodimos
406   et al., 2004; Redding and Greene, 2013). Indeed, the surface charge of proteins strongly affects their
407   mobility in cells (Elowitz et al., 1999; Schavemaker et al., 2017), and high intracellular salt
408   concentrations can disrupt DNA-binding *in vivo (Cagliero and Jin, 2013)*. The abundance of non-
409   specific binding also suggests that the percentage of the chromosome occupied by proteins may be
410   higher than expected. Based on the combined percentage of DNA-bound proteins (both specific and
411   non-specific) in Table 1, together with literature estimates of their copy number and DNA footprint, we
412   estimate that at any given time 28% of the chromosome is occupied by the 11 proteins studied (12%
413   long-lived binding and 16% transient binding, see Methods). These proteins represent just a fraction of
414   all DNA-binding proteins, suggesting the total DNA occupancy of the entire proteome is substantially
415   higher. This high occupancy, or chromosome-crowding, highlights the importance of studying protein-
416   DNA interaction in the native cellular environment. Besides the target search, non-specific DNA

417   binding likely also influences the dissociation of proteins from their specific target sites. Several studies

418   have shown that competition with proteins in solution accelerates DNA unbinding due to invasion of a

419   partially-dissociated state (Chen et al., 2015; Gibb et al., 2014; Graham et al., 2011; Loparo et al., 2011).

420   Although this has been demonstrated for exchanges between identical proteins in solution and on DNA,

421   the overwhelming abundance of other DNA-binding proteins and their frequent transient associations

422   with DNA likely contribute significantly to the turnover of DNA-bound proteins in vivo. Thus, non-

423   specific DNA interactions play a crucial role in both the search and the dissociation of DNA-binding

424   proteins.

425   Beyond these fundamental implications, our chromosome-degradation system has broader potential

426   applications in synthetic biology and has benefits compared to alternative approaches such as

427   chromosome-free minicells. Minicells can be generated by forcing aberrant cell divisions close to the

428   cell poles, however these cells have a perturbed makeup of proteins and contain few DNA binding

429   proteins (Shepherd et al., 2001). In contrast, our chromosome-degraded cells retain the DNA binding

430   proteins and maintain the same cell size and geometry. Moreover, we have shown that DNA-free *E.

431   coli* cells maintain ATP levels and continue to produce plasmid-encoded proteins for several hours,

432   enabling targeted expression of exogenous genes without interference from chromosomal gene

433   expression. Removing all endogenous gene circuitry from *E. coli* cells but maintaining the transcription

434   machinery provides customizable non-viable containers for a range of applications, including

435   expression of synthetic gene circuits, biosensing, and drug delivery (Caliando and Voigt, 2015; Fan et

436   al., 2020; MacDiarmid et al., 2007; Rampley et al., 2017).

437

438   **Methods**

439   **Bacterial strains, plasmids and growth**

440   Bacterial strains and plasmids are listed in Table S1. All experiments were performed in *E. coli* TB28

441   background strain (MG1655 *ΔlacIZYA*) (Bernhardt and de Boer, 2005). PAmCherry fusion proteins

442   expressed from their endogenous chromosome loci were previously characterized: RNAP, HU and HN-

443   S (Stracy et al., 2015), LacI (Garza de Leon et al., 2017), Pol1 and LigA (Uphoff et al., 2013),

444   UvrA (Stracy et al., 2016), MutS (Uphoff et al., 2016), ParC (Zawadzki et al., 2015), MukB

445   (Badrinarayanan et al., 2012), GyrA (Stracy et al., 2019). Fusions were moved to *E. coli* TB28 strain

446   by P1 transduction. Construction of plasmids expressing LacI-PAmCherry or LacI mutant are described

447   in (Garza de Leon et al., 2017). Unconjugated PAmCherry was produced from the plasmid pBAD\HisB

448   PAmCherry1 (Endesfelder et al., 2013). ParB-mCherry was produced from pSN70 plasmid (Nolivos et

449   al., 2019). The *I-SceI* cut site (*I-SceI^{CS}*) is followed by *cat* gene (chloramphenicol resistance) flanked

450   by *frt* sites as described previously (Lesterlin et al., 2013). *I-SceI^{CS}* was inserted in two chromosome

451   loci by λ-Red recombination (Datsenko and Wanner, 2000); *ilvA* (3953 kb) close to the origin of

452   replication, and *ydeO* (1580 kb) in the *terminus* region. Using sequential P1 transduction, we

453   constructed the OT strain (for *Ori-Ter*) carrying *ilvA::I-SceI^{CS}* and *ydeO::I-SceI^{CS}*. After each

454   transduction round, the *cat* gene was removed using Pcp20 plasmid (Datsenko and Wanner, 2000). P1

455   transduction was also used to transfer *recA-* mutation *recAT233C-Tet* or *minC-Ypet* allele (Bisicchia et

456   al., 2013) alleles. Unless otherwise stated, cells were grown at 30°C in M9 medium supplemented with

457   glucose (0.2%). When appropriate, growth media were supplemented with Ampicillin (Ap) 100 µg/ml,

458   Chloramphenicol (Cm) 20 µg/ml or Kanamycin (Kn) 50 µg/ml.

459

460   **Sample preparation for microscopy**

461   OT strains carrying two *I-SceI^{CS}* were transformed with pSN1 plasmid carrying the *I-SceI* gene under

462   the control of the P_{lac} promoter and plated on LB agarose plates containing 0.2 % glucose and ampicillin

463   at 30ºC. Transformant clones were propagated on LB agarose plates containing 0.2 % glucose and

464   ampicillin. Transformation was performed *de novo* before each experiment since strains carrying *I-*

465   *SceI^{CS}* and the pSN1 plasmid exhibit genetic instability due to leaky *I-SceI* expression causing

466   unrepairable DNA double-stranded breaks in the *recA-* strain. For each strain, a single colony was

467   inoculated in M9 minimal medium supplemented with 0.2% glucose and ampicillin and incubated

468   overnight at 30ºC with agitation (140 rpm). The next day, overnight cultures were diluted and grown to

469   early exponential phase ($OD_{600nm} \sim 0.2$). 0.2% arabinose was added to induce the production of I-SceI

470   endonuclease and initiate chromosome degradation in the *recA-* strains. Cultures were incubated at 30ºC

471   with agitation for the duration indicated in the text and figures (120 min for complete DNA degradation)

472   before microscopy. For control experiments in fixed cells, 2.5% paraformaldehyde was added to the

473   growth media for 1 hour prior to imaging. Cell filamentation was induced by addition of cephalexin at

474   final concentration of 5 µg/ml.

475   The cell suspension was concentrated by centrifugation (benchtop centrifuge at 6000 rpm), removal of

476   the supernatant and resuspension in 1/10th of the initial sample volume. Cells were immobilized on pads

477   of 1% low-fluorescence agarose (Biorad) in M9 medium with 0.2% glucose as previously described

478   (Lesterlin and Duabrry, 2016). For PALM microscopy 0.17 mm thickness coverslips were heated in an

479   oven to 500°C to remove any background fluorescent particles before use. For quantification of

480   chromosome degradation and MinC-Ypet oscillation by wide-field epifluorescence imaging, DNA

481   staining was performed by incubating the cell suspension for 15 min with 2 4',6-diamidino-2-

482   phenylindole (DAPI) at 4 µg/ml prior to cell concentration and imaging. For multi-color imaging of the

483   nucleoid and PAmCherry fusions, we stained DNA with 500 nM SytoGreen for 15 min before imaging

484   (because DAPI excitation would cause photoactivation of PAmCherry).

485

486   **Wide-field epifluorescence microscopy imaging**

487   Wide-field epifluorescence microscopy imaging of DAPI-stained cells was carried out on an Eclipse

488   Ti-E microscope (Nikon), equipped with 100s/1.45 oil Plan Apo Lambda phase objective, Flash4 V2

489 CMOS camera (Hamamatsu), and using NIS Elements software for image acquisition. Acquisition was

490 performed in phase contrast and epifluorescence mode using 50% power of a Fluo LED Spectra X light

491 source at 405 nm and 560 nm excitation wavelengths for DAPI and ParB-mCherry, respectively.

492 Wide-field imaging of MinC-Ypet was carried out on a Nikon Eclipse TE2000-U microscope equipped

493 with a 100X objective, CCD camera (Cool-SNAP by Photometrics) and Metamorph 6.2 acquisition

494 software. Time-lapse movies were acquired in phase contrast and epifluorescence at 2-s intervals with

495 50 ms exposure for MinC-Ypet at 30ºC.

496

497 *Widefield epifluorescence image analysis*

498 Cells were automatically detected using the MicrobeJ plugin for Fiji (Ducret et al., 2016). Intracellular

499 DAPI or ParB-mCherry mean fluorescence intensity (a.u.) was automatically extracted and plotted

500 using the MicrobeJ results interface. For analysis of MinC oscillation, cells were outlined using the

501 MATLAB-based tool MicrobeTracker (Sliusarenko et al., 2011). The fluorescence signal was

502 integrated across the cross-section of each cell to generate a one-dimensional fluorescence profile in

503 each frame. The fluorescence signal was normalized to the total fluorescence in each frame to remove

504 photobleaching effects and facilitate MinC-Ypet localization analysis. The fluorescence signals

505 obtained from each cell were further analyzed by generating kymographs using custom MATLAB code.

506 The width of the kymograph corresponds to the cell length L. We integrated the fluorescence intensity

507 for both cell halves at in each frame,

508
$$F_{x,left}(t) = \int_{x=0}^{L/2} f(x,t)dx \qquad F_{x,right}(t) = \int_{x=L/2}^{L} f(x,t)dx$$

509 By fitting the data to a trigonometric function the oscillation period is calculated from the angular

510 frequency $\omega = \frac{2\pi}{T}$

511
$$F_{x,\genfrac{}{}{0pt}{}{left}{right}}(t) = a \cdot \cos(\omega \cdot t) + b \cdot \sin(\omega \cdot t)$$

512 The time-averaged concentration profile of MinC is obtained by integration of the entire kymograph

513 over all frames,

514
$$F_t(x) = \int_t f(x,t)dt$$

515 For analyzing MinC oscillations in filamentous cells, a slightly modified kymograph analysis was used.

516 The MinC concentration profile was determined as described above. The positions of the fluorescence

517 minima *xmin* were used to split the kymographs into several stripes. The overall oscillation period *Tm*

518 was calculated as the average of all oscillation periods determined for each stripe in the kymograph.

519 The oscillation wavelength was determined from the distance between two neighboring peaks.

520 Depending on the length of the cell and the number of oscillations a set of wavelengths was determined

521 from which a mean wavelength was calculated as

522
$$\lambda = \frac{1}{n}\sum_{i=1}^{n}\left(x_{min,i+1} - x_{min,i}\right)$$

523 Where the number n of oscillations corresponds to the number of peaks – 1.

524

525 **Live-cell photoactivated single-molecule tracking**

526 Live cell photoactivated single-molecule tracking was performed on a custom-built total internal

527 reflection fluorescence (TIRF) microscope built around the Rapid Automated Modular Microscope

528 (RAMM) System (ASI Imaging) as previously described (Uphoff, 2016). PAmCherry activation was

529 controlled by a 405 nm laser and excited with 561 nm. All lasers were provided by a multi-laser engine

530 (iChrome MLE, Toptica). At the fiber output, the laser beams were collimated and focused (100x oil

531 immersion objective, NA 1.4, Olympus) onto the sample under an angle allowing for highly inclined

532 thin illumination (Tokunaga et al., 2008). Fluorescence emission was filtered by a dichroic mirror and

533 filter (ZT405/488/561rpc & ZET405/488/561NF, Chroma). PAmCherry emission was projected onto

534 an EMCCD camera (iXon Ultra, 512x512 pixels, Andor). The pixel size was 96 nm. Transmission

535 illumination was provided by an LED source and condenser (ASI Imaging and Olympus). Sample

536 position and focus were controlled with a motorized piezo stage, a z-motor objective mount, and

537 autofocus system (MS-2000, PZ-2000FT, CRISP, ASI Imaging). Movies were acquired under

538 continuous laser excitation with exposure times of 15 ms or 5 ms for 20,000 frames at 20ºC. Camera

539 readout was 0.48 ms giving frame intervals of 15.48 ms or 5.48 ms, respectively. We also recorded a

540 transmitted light snapshot for segmenting cells in each movie. For imaging SytoGreen, snapshots with

541 488 nm excitation with a 50 ms exposure time were acquired prior to PAmCherry imaging.

542

543 *Localization and tracking*

544 Single-molecule-tracking analysis was performed using custom-written MATLAB software

545 (MathWorks) as previously described (Uphoff et al., 2014): fluorophore images were identified for

546 localization by band-pass filtering and applying an intensity threshold to each frame of the movie.

547 Candidate positions were used as initial guesses in a two-dimensional elliptical Gaussian fit for high-

548 precision localization. Free fit parameters were x-position, y-position, x-width, y-width, elliptical

549 rotation angle, intensity, background. Localizations were segmented based on cell outlines obtained

550 from MicrobeTracker applied to the brightfield snapshots. Single-particle tracking analysis was

551 performed by adapting the MATLAB implementation of the algorithm described in (Crocker and Grier,

552 1996). Positions were linked to a track if they appeared in consecutive frames within a window of 5

553 pixels (0.48 µm). When multiple localizations fell within the tracking window, tracks were linked such

554 that the sum of step distances was minimized. We used a 'memory' parameter of 1 frame to allow for

555 transient disappearance of the fluorophore within a track due to blinking or missed localization.

556

557 *Measuring the diffusion of tracked molecules*

558 We determined the mobility of each molecule by calculating an individual apparent diffusion

559 coefficient, D_i^*, from the one-step mean-squared displacement (MSD) of the track using:

560

561
$$D_i^* = \frac{1}{4n\Delta t} \sum_{i=1}^{n} [x(i\Delta t) - x(i\Delta t + \Delta t)]^2 + [y(i\Delta t) - y(i\Delta t + \Delta t)]^2$$

562

563 Where $x(t)$ and $y(t)$ are the coordinates of the molecule at time t, the frame time of the camera is Δt,

564 and n is the number of frames over which the molecule is tracked. For a molecule diffusing with an

565 apparent diffusion coefficient D^*, the probability of measuring a D_i^* by tracking it over n frames, is

566 given by (Vrljic et al., 2002):

567

568

569
$$p(D_i^*) = \frac{1}{(n-1)!} * \left(\frac{n}{D}\right)^n * (D_i^*)^{n-1} * exp\left(\frac{-nD_i^*}{D}\right)$$

570

571 In order to determine the apparent diffusion coefficient, D^*, from the population of individual single-

572 molecule D_i^* values, longer tracks were truncated after 5th localization (i.e. $n = 4$). The D_i^* distribution

573 was then fitted with the equation for $n = 4$:

574
$$p(D_i^*) = \frac{1}{6} * \left(\frac{4}{D}\right)^4 * (D_i^*)^3 * exp\left(\frac{-4D_i^*}{D}\right)$$

575

576 Fits were performed using maximum likelihood estimation in MATLAB. For unperturbed cells the

577 protein diffusion distributions were fit with a model containing two molecular species with diffusion

578 coefficients D_1^* and D_2^*: representing immobile molecules bound to DNA for the entire trajectory, and

579 mobile molecules diffusing and binding only transiently to DNA:

580
$$p(D_i^*) = \left[\frac{A_1}{6} * \left(\frac{4}{D_1^*}\right)^4 * (D_i^*)^3 * exp\left(\frac{-4D_i^*}{D_1^*}\right)\right] + \left[\frac{(1-A)}{6} * \left(\frac{4}{D_2^*}\right)^4 * (D_i^*)^3 * exp\left(\frac{-4D_i^*}{D_2^*}\right)\right]$$

581

582 where A and $1 - A$ are the fraction of molecules found in each state. The localization uncertainty, σ_{loc},

583 manifests itself as a positive offset of $\sigma_{loc}^2/\Delta t$ in the D^* value (Michalet and Berglund, 2012). Based on

584 the estimated localization uncertainty of ~35 nm for our measurements, we expected a positive shift in

585 the mean D^* value of immobile molecules to ~0.7 $\mu m^2 s^{-1}$. Where indicated error bars represent 95%

586 confidence intervals obtained from fitting the D* distribution for 1000 bootstrap resamplings with

587 replacement of individual segmented cells. For each bootstrap the tracks within the sampled cells were

588 pooled and fitted as described above.

589

590   To plot maps of tracks from mobile and immobile molecules, we used a threshold of 0.15 $\mu m^2 s^{-1}$ to

591   separate the populations.

592

593   *Monte Carlo diffusion simulations*

594   The apparent diffusion coefficients determined experimentally through particle tracking do not take

595   into account three-dimensional confinement in the bacterial cell. We followed a similar rationale as

596   before to remove this bias (Uphoff et al., 2013): we simulated Brownian motion confined within 3D

597   cell volumes obtained from the segmented 2D brightfield images. The distance from the midline to the

598   cell edge was used as the radius of a cylindrical volume for each length segment of a cell. For each cell

599   diffusion simulations of the same number of molecules as measured experimentally were performed.

600   Each 15 ms frame was split into 100 sub-frames with Gaussian-distributed displacements in each sub-

601   frame. Each molecule trajectory was given a random starting time to mimic stochastic photoactivation,

602   and a duration sampled from an exponential distribution with a mean time equal to our experimentally

603   determined photobleaching lifetime (85 ms). The sub-frame distributions were then averaged to give a

604   position for each frame, and a localization error sampled from a Gaussian distribution with σ_{loc} = 35

605   nm was added. The list of simulated localizations, with their corresponding frame numbers was then

606   analyzed using the same algorithms with the same settings as for experimental data. The best estimate

607   for the unbiased diffusion coefficient was determined by running the simulations for different D values

608   between 0 and 10 $\mu m^2 s^{-1}$ and selecting inputted D value from the simulated D^* distribution which best

609   approximates (based on the least squares error) the experimentally obtained D^* distribution. Since

610   diffusion coefficients in DNA-free cells were much higher than in unperturbed cells we also performed

611   experiments and simulations for Pol1 and MukB at 5.48 ms exposure times to verify the same

612   underlying unbiased diffusion coefficients were obtained independent of the data acquisition

613   conditions. 95% confidence intervals were estimated by fitting the experimental D^* distribution for

614   1000 bootstrap resamplings with replacement of individual segmented cells as described previously.

615   Simulations were then performed to determine inputted D value which best approximates the higher

616   and lower confidence bounds from the experimentally determined D^* values.

617

618   We hypothesized that the observed diffusion of DNA-binding proteins in unperturbed cells represented

619   mobile molecules interconverting between D_{free} and D_{bound} states. By comparing diffusion in

620   unperturbed and DNA-free cells, it is possible to estimate the relative occupation of the states but not

621   the absolute duration a molecule spends in each state. To simulate molecules interconverting between

622   these states, we used the D_{free} value based on the simulations of DNA-free cells, and a D_{bound} value of

623   0.04 $\mu m^2 s^{-1}$. Because the D_{mobile} population appears as a single species the interconversions must occur

624   on a timescale below the observation window per track (75 ms, 5 frames of 15 ms). We therefore

625   simulated the duration of D_{bound}, t_{bound}, by randomly sampling from an exponential distribution with a

626   mean of 1 ms. We performed simulations for a range of ratios of durations in the D_{free} and D_{bound} states

627   by varying, t_{free}, the duration of free diffusion between binding events. Using least squares optimization,

628   we determined the ratio which best recapitulated the experimental D^*_{mobile} value determined from fitting

629   the experimental D* distribution.

630

631   *Chromosome occupancy calculations*

632   To estimate the percentage of the chromosome occupied by proteins we used literature estimates of the

633   DNA footprint of each protein. RNAP (70bp, (Ross and Gourse, 2005); HU (36bp, Gruber, 2014); H-

634   NS (30bp; van der Valk et al., 2017); DNA gyrase (100bp, Reece and Maxwell, 1991). Where no

635   DNA footprint estimates could be found we assumed a footprint of 10bp. The total bp occupied was

636   calculated by the molecules/cell multiplied by the total fraction binding (including stable binding and

637   transient binding) in Table 1, and the DNA footprint, giving 1.96Mb of DNA. Under the minimal media

638   growth conditions in this study there are on average 1.5 chromosomes per cell, totaling 6.9Mb of DNA

639   (Wang et al., 2005).

640

Table 1. Quantitative partitioning of DNA-binding protein activity

Protein	Function	Size of PAmCherry labelled protein or protein complex (kDa)[1]	Molecules/ cell	D^*_{mobile} ($\mu m^2/s$)	D_{free} ($\mu m^2/s$)	% of long-lived DNA-bound molecules	% transient DNA- bound molecules	% freely diffusing molecules	Copy number reference
RNA Polymerase (β' subunit)	transcription	480 (holoenzyme)	4,000	0.36 ± 0.01	2.7 ± 0.1	45 ± 2	48 ± 2	7 ± 1	(Bakshi et al., 2013; Stracy et al., 2015)
DNA polymerase 1 (PolA)	DNA repair / replication	128 (monomer)	500	1.05 ± 0.01	6.6 ± 0.2	4 ± 1	61± 2	35 ± 2	(Uphoff et al., 2013)
MukBEF (MukB subunit)	chromosome organization/	1000 (dimer)	100	0.44 ± 0.01	1.2 ± 0.1	58 ± 2	24 ± 1	18 ± 1	(Badrinarayanan et al., 2012)
DNA Ligase (LigA)	DNA repair / replication	102 (monomer)	100	1.22 ± 0.02	6.9 ± 0.3	7 ± 1	56 ± 2	37 ± 2	(Uphoff et al., 2013)
Lac repressor (LacI)	gene regulation	220 (tetramer)	40	0.40 ± 0.01	3.3 ± 0.2	41 ± 3	55 ± 3	4 ± 1	(Garza de Leon et al., 2017)
Heat Unstable protein (HU)	nucleoid associated protein/ gene regulation	48 (heterodimer)	30,000	0.33 ± 0.01	12.6 ± 4.8[†]	23 ± 1	76 ± 1[†]	0.8 ± 2[†]	(Gruber, 2014)
Histone-like nucleoid structuring protein (H-NS)	nucleoid associated protein/ gene regulation	87 (dimer)	20,000	0.41 ± 0.01	8.0 ± 2.2[†]	73 ± 2	27 ± 2[†]	0.3 ± 1[†]	(Katayama et al., 1996)
MutS	DNA repair	248 (dimer)	100	0.37 ± 0.01	3.7 ± 1.7[†]	26 ± 2	69 ± 7[†]	5 ± 1[†]	(Uphoff et al., 2016)
Topoisomerase IV (ParC subunit)	Supercoiling/ decatenation	366 (heterotetramer)	80	0.40 ± 0.01	2.7 ± 1.8[†]	37 ± 2	52 ± 18[†]	11 ± 7[†]	(Zawadzki et al., 2015)

UvrA	DNA repair	270 (dimer)	80	0.38 ± 0.02	$3.4 \pm 1.7^{\dagger}$	43 ± 2	$51 \pm 8^{\dagger}$	$6 \pm 18^{\dagger}$	(Stracy et al., 2016)
DNA gyrase (GyrA subunit)	Supercoiling	424 (heterotetramer)	600	0.35 ± 0.01	$2.4 \pm 1.8^{\dagger}$	55 ± 1	$39 \pm 17^{\dagger}$	$7 \pm 8^{\dagger}$	(Stracy et al., 2019)

[1]Note that in some cases the functional complex contains more than one copy of the subunit which has been labelled, and the complex therefore contains more than one PAmCherry protein. †Denotes predicted values based on extrapolation of D_{free} values in shown in Fig. 6.

Figures Legends

Figure 1. Intracellular mobility of diverse types of DNA-binding proteins in live *E. coli* cells is highly variable and unrelated to their molecular weights. (A) Illustration of photoactivated single-molecule tracking, showing example fluorescence images and trajectories of a mobile molecule (top) and immobile molecule (bottom) within the cell (green outline). Scale bar 1 µm. (B) Histograms of apparent diffusion coefficients D* (grey bars) for diverse DNA-binding proteins, fitted with a model (black dashed line) of a mixture of immobile (red) and mobile molecules (blue). The number of cells ($n_c =$) and the numbers of tracks ($n_t =$) analyzed are indicated. (C) Percentages of long-lived binding molecules obtained from fitting D* histograms in Fig. 1 with a model of a mixture of immobile and mobile molecules. Error bars represent 95% confidence intervals. (D) D_{mobile}* values for the mobile molecule populations. (E) D_{mobile}* plotted against the cubic root of the molecular weight of the protein complex.

Figure 2. DNA-binding proteins stay closely associated with the nucleoid during the target search. (A) Localizations of Pol1 (PolA-PAmCherry), (B) RNAP (RpoC-PAmCherry), and (C) ribosomal protein S1 (S1-PAmCherry) molecules relative to the nucleoid. From left to right: transmitted light image (scale bar 1 µm); SytoGreen-stained nucleoid DNA with segmented cell outline; maps showing the tracks of mobile (blue) and immobile (red) PAmCherry fusion proteins in cells. Histograms show localizations across the long cell axis (blue/red bars) together with the SytoGreen fluorescence profile of the nucleoid (green line). (B) Average spatial distributions of Pol1, RNAP and ribosomal protein S1 immobile and mobile molecules.

Figure 3. Generating chromosome-free cells that remain metabolically active. (A) Schematic of the chromosome-degradation system. The production of I-SceI endonuclease induces the formation of two double-stranded-breaks (DSBs) at *I-SceI* cut-sites inserted at diametrically opposed position on the chromosome. In a *recA-* mutant strain, processing of the two DSBs by RecBCD complexes results in the complete degradation of the chromosome. (B) Chromosome degradation following I-SceI induction is revealed by the loss of DAPI-stained DNA fluorescence (blue) in cells with FM464-labelled membrane (red). Scale bar, 1 µm. (C) Distributions of DAPI fluorescence shows complete chromosome degradation 120 min after I-SceI induction (black dot: mean and outliers, horizontal lines: median, 1st and 3rd quartiles). The number of cells analyzed (n) is indicated. (D) MinC-YPet oscillation in an example chromosome-free cell. Cell filamentation was induced by cephalexin treatment. Transmitted light, DAPI, and MinC-YPet fluorescence images (2 s/frame time lapse) obtained 120 min post I-SceI induction. Scale bar, 1 µm. (E) Kymograph of MinC-YPet oscillation in an example cephalexin-treated

filamentous cell. The width of the kymograph corresponds to the cell long-axis (L). Time-dependent intensity signals in the cell halves are shown in blue and green with the oscillation period T_m. Time-average concentration profile shown underneath for measuring the oscillation wavelength. (F, G) MinC-YPet oscillation period and wavelength are similar in filamentous cells with and without chromosome degradation. The number of cells analyzed (n) is indicated.

Figure 4. Diffusion of lac repressor increases in chromosome-free cells. (A) D* histograms of LacI-PAmCherry in unperturbed cells (left) fitted with a model (black dashed line) of a mixture of immobile (red) and mobile molecules (blue). D* distribution of LacI-PAmCherry in chromosome-free cells 120 min after I-SceI induction (right) fitted with a model for mobile molecules (green).). (B) Mean squared displacement plots corresponding to data in panels (A) and (D). (C) Cumulative distributions of the step lengths between consecutive localizations in unperturbed and in chromosome-free cells for LacI-PAmCherry, LacI[41]-PAmCherry, and unconjugated PAmCherry. The distributions shift to longer steps with increasing diffusion coefficient. (D) D* histograms of mutant LacI[41]-PAmCherry in unperturbed cells (left) and in chromosome-free cells 120 min after I-SceI induction (right) fitted with a model for mobile molecules (purple and magenta, respectively.

Figure 5. Chromosome degradation increases the mobility of diverse types of DNA-binding proteins. (A) Diagrams of RNAP, Pol1, MukB and Ligase DNA-binding properties. (B) Tracks of RNAP-PAmCherry, Pol1-PAmCherry, MukB-PAmCherry and LigA-PAmCherry in example cells, with the color of each track representing its D* value. D* histograms in cells without I-SceI induction, fitted with a model of a mixture of immobile (red) and mobile (blue) molecules. (B) Tracks of RNAP-PAmCherry, Pol1-PAmCherry, MukB-PAmCherry and LigA-PAmCherry in example chromosome-free cells 120 min after I-SceI induction with the color of each track representing its D* value. D* histograms in chromosome-free cells fitted with a model for mobile molecules. The number of cells (n_c =) and the numbers of tracks (n_t =) analyzed are indicated in B and C.

Figure 6. Quantitative partitioning of protein states. (A) Illustration of Brownian motion simulation to estimate unbiased diffusion coefficients D_{mobile} (in unperturbed cells) and D_{free} (in chromosome-free cells). (B) D_{mobile} and D_{free} plotted *vs* molecular weight M on log-scale. Linear fit $\log(D_{free}) = \alpha \cdot \log(c \cdot M)$. (C) Partitioning long-lived DNA-binding (orange), transient DNA-binding (purple), and 3D diffusion (blue) states for RNAP and (D) for LacI, Pol1, LigA and MukB. (E) The percentage of search time spent nonspecifically bound to DNA for all 11 DNA-binding proteins studied. Blue bars show the

proteins with D_{free} measured in chromosome-free cells, grey bars show proteins with D_{free} estimated from the fit in panel B. Error bars correspond to standard deviations.

REFERENCES

Bacia, K., Kim, S.A., and Schwille, P. (2006). Fluorescence cross-correlation spectroscopy in living cells. Nat Methods *3*, 83–89.

Badrinarayanan, A., Reyes-Lamothe, R., Uphoff, S., Leake, M.C., and Sherratt, D.J. (2012). In vivo architecture and action of bacterial structural maintenance of chromosome proteins. Science *338*, 528–531.

Bakshi, S., Bratton, B.P., and Weisshaar, J.C. (2011). Subdiffraction-limit study of Kaede diffusion and spatial distribution in live Escherichia coli. Biophys. J. *101*, 2535–2544.

Bakshi, S., Dalrymple, R.M., Li, W., Choi, H., and Weisshaar, J.C. (2013). Partitioning of RNA Polymerase Activity in Live Escherichia coli from Analysis of Single-Molecule Diffusive Trajectories. Biophys J *105*, 2676–2686.

Bernhardt, T.G., and de Boer, P.A.J. (2005). SlmA, a nucleoid-associated, FtsZ binding protein required for blocking septal ring assembly over Chromosomes in E. coli. Mol. Cell *18*, 555–564.

Bisicchia, P., Arumugam, S., Schwille, P., and Sherratt, D. (2013). MinC, MinD, and MinE Drive Counter-oscillation of Early-Cell-Division Proteins Prior to Escherichia coli Septum Formation. MBio *4*.

Cabrera, J.E., Cagliero, C., Quan, S., Squires, C.L., and Jin, D.J. (2009). Active Transcription of rRNA Operons Condenses the Nucleoid in Escherichia coli: Examining the Effect of Transcription on Nucleoid Structure in the Absence of Transertion. J Bacteriol *191*, 4180–4185.

Cagliero, C., and Jin, D.J. (2013). Dissociation and re-association of RNA polymerase with DNA during osmotic stress response in Escherichia coli. Nucleic Acids Res. *41*, 315–326.

Caliando, B.J., and Voigt, C.A. (2015). Targeted DNA degradation using a CRISPR device stably carried in the host genome. Nat Commun *6*, 6989.

Chen, T.-Y., Santiago, A.G., Jung, W., Krzemiński, Ł., Yang, F., Martell, D.J., Helmann, J.D., and Chen, P. (2015). Concentration- and chromosome-organization-dependent regulator unbinding from DNA for transcription regulation in living cells. Nat Commun *6*, 7445.

Chow, E., and Skolnick, J. (2017). DNA Internal Motion Likely Accelerates Protein Target Search in a Packed Nucleoid. Biophys J *112*, 2261–2270.

Cluzel, P., Surette, M.G., and Leibler, S. (2000). An ultrasensitive bacterial motor revealed by monitoring signaling proteins in single cells. Science *287*, 1652–1655.

Crocker, J.C., and Grier, D.G. (1996). When Like Charges Attract: The Effects of Geometrical Confinement on Long-Range Colloidal Interactions. Phys. Rev. Lett. *77*, 1897–1900.

Datsenko, K.A., and Wanner, B.L. (2000). One-step inactivation of chromosomal genes in Escherichia coli K-12 using PCR products. Proc. Natl. Acad. Sci. U.S.A. *97*, 6640–6645.

Di Ventura, B., Knecht, B., Andreas, H., Godinez, W.J., Fritsche, M., Rohr, K., Nickel, W., Heermann, D.W., and Sourjik, V. (2013). Chromosome segregation by the Escherichia coli Min system. Mol Syst Biol *9*, 686.

Ducret, A., Quardokus, E.M., and Brun, Y.V. (2016). MicrobeJ, a tool for high throughput bacterial cell detection and quantitative analysis. Nat Microbiol *1*, 16077.

Dworsky, P., and Schaechter, M. (1973). Effect of Rifampin on the Structure and Membrane Attachment of the Nucleoid of Escherichia coli. J Bacteriol *116*, 1364–1374.

Elf, J., Li, G.-W., and Xie, X.S. (2007). Probing transcription factor dynamics at the single-molecule level in a living cell. Science *316*, 1191–1194.

Elmore, S., Müller, M., Vischer, N., Odijk, T., and Woldringh, C.L. (2005). Single-particle tracking of oriC-GFP fluorescent spots during chromosome segregation in Escherichia coli. J. Struct. Biol. *151*, 275–287.

Elowitz, M.B., Surette, M.G., Wolf, P.E., Stock, J.B., and Leibler, S. (1999). Protein mobility in the cytoplasm of Escherichia coli. J. Bacteriol. *181*, 197–203.

Endesfelder, U., Finan, K., Holden, S.J., Cook, P.R., Kapanidis, A.N., and Heilemann, M. (2013). Multiscale spatial organization of RNA polymerase in Escherichia coli. Biophys. J. *105*, 172–181.

English, B.P., Hauryliuk, V., Sanamrad, A., Tankov, S., Dekker, N.H., and Elf, J. (2011). Single-molecule investigations of the stringent response machinery in living bacterial cells. Proc. Natl. Acad. Sci. U.S.A. *108*, E365-373.

Erbaş, A., and Marko, J.F. (2019). How do DNA-bound proteins leave their binding sites? The role of facilitated dissociation. Current Opinion in Chemical Biology *53*, 118–124.

Erbaş, A., Cruz, M.O. de la, and Marko, J.F. (2019). Receptor-Ligand Rebinding Kinetics in Confinement. Biophysical Journal *116*, 1609–1624.

Fan, C., Davison, P.A., Habgood, R., Zeng, H., Decker, C.M., Salazar, M.G., Lueangwattanapong, K., Townley, H.E., Yang, A., Thompson, I.P., et al. (2020). Chromosome-free bacterial cells are safe and programmable platforms for synthetic biology. PNAS *117*, 6752–6761.

Feig, M., Harada, R., Mori, T., Yu, I., Takahashi, K., and Sugita, Y. (2015). Complete atomistic model of a bacterial cytoplasm for integrating physics, biochemistry, and systems biology. J. Mol. Graph. Model. *58*, 1–9.

Gahlmann, A., and Moerner, W.E. (2014). Exploring bacterial cell biology with single-molecule tracking and super-resolution imaging. Nat. Rev. Microbiol. *12*, 9–22.

Garza de Leon, F., Sellars, L., Stracy, M., Busby, S.J.W., and Kapanidis, A.N. (2017). Tracking Low-Copy Transcription Factors in Living Bacteria: The Case of the lac Repressor. Biophys. J. *112*, 1316–1327.

Gibb, B., Ye, L.F., Gergoudis, S.C., Kwon, Y., Niu, H., Sung, P., and Greene, E.C. (2014). Concentration-dependent exchange of replication protein A on single-stranded DNA revealed by single-molecule imaging. PLoS ONE *9*, e87922.

Graham, J.S., Johnson, R.C., and Marko, J.F. (2011). Concentration-dependent exchange accelerates turnover of proteins bound to double-stranded DNA. Nucleic Acids Res. *39*, 2249–2259.

Gray, W.T., Govers, S.K., Xiang, Y., Parry, B.R., Campos, M., Kim, S., and Jacobs-Wagner, C. (2019). Nucleoid Size Scaling and Intracellular Organization of Translation across Bacteria. Cell *177*, 1632-1648.e20.

Gruber, S. (2014). Multilayer chromosome organization through DNA bending, bridging and extrusion. Curr. Opin. Microbiol. *22*, 102–110.

Halford, S.E., and Marko, J.F. (2004). How do site-specific DNA-binding proteins find their targets? Nucleic Acids Res. *32*, 3040–3052.

Hammar, P., Leroy, P., Mahmutovic, A., Marklund, E.G., Berg, O.G., and Elf, J. (2012). The lac repressor displays facilitated diffusion in living cells. Science *336*, 1595–1598.

Hasnain, S., McClendon, C.L., Hsu, M.T., Jacobson, M.P., and Bandyopadhyay, P. (2014). A new coarse-grained model for E. coli cytoplasm: accurate calculation of the diffusion coefficient of proteins and observation of anomalous diffusion. PLoS ONE *9*, e106466.

Hippel, P.H. von, and Berg, O.G. (1989). Facilitated target location in biological systems. J. Biol. Chem. *264*, 675–678.

Hu, Z., Gogol, E.P., and Lutkenhaus, J. (2002). Dynamic assembly of MinD on phospholipid vesicles regulated by ATP and MinE. Proc. Natl. Acad. Sci. U.S.A. *99*, 6761–6766.

Joyce, C.M., and Steitz, T.A. (1994). Function and structure relationships in DNA polymerases. Annu. Rev. Biochem. *63*, 777–822.

Kalodimos, C.G., Biris, N., Bonvin, A.M.J.J., Levandoski, M.M., Guennuegues, M., Boelens, R., and Kaptein, R. (2004). Structure and Flexibility Adaptation in Nonspecific and Specific Protein-DNA Complexes. Science *305*, 386–389.

Kalwarczyk, T., Tabaka, M., and Holyst, R. (2012). Biologistics--diffusion coefficients for complete proteome of Escherichia coli. Bioinformatics *28*, 2971–2978.

Kao-Huang, Y., Revzin, A., Butler, A.P., O'Conner, P., Noble, D.W., and von Hippel, P.H. (1977). Nonspecific DNA binding of genome-regulating proteins as a biological control mechanism: measurement of DNA-bound Escherichia coli lac repressor in vivo. Proc. Natl. Acad. Sci. U.S.A. *74*, 4228–4232.

Kapanidis, A.N., Uphoff, S., and Stracy, M. (2018). Understanding Protein Mobility in Bacteria by Tracking Single Molecules. J. Mol. Biol. *430*, 4443–4455.

Katayama, T., Takata, M., and Sekimizu, K. (1996). The nucleoid protein H-NS facilitates chromosome DNA replication in Escherichia coli dnaA mutants. J. Bacteriol. *178*, 5790–5792.

Konopka, M.C., Shkel, I.A., Cayley, S., Record, M.T., and Weisshaar, J.C. (2006). Crowding and confinement effects on protein diffusion in vivo. J. Bacteriol. *188*, 6115–6123.

Kumar, M., Mommer, M.S., and Sourjik, V. (2010). Mobility of cytoplasmic, membrane, and DNA-binding proteins in Escherichia coli. Biophys. J. *98*, 552–559.

Kuznetsova, I.M., Turoverov, K.K., and Uversky, V.N. (2014). What macromolecular crowding can do to a protein. Int J Mol Sci *15*, 23090–23140.

Landgraf, D., Okumus, B., Chien, P., Baker, T.A., and Paulsson, J. (2012). Segregation of molecules at cell division reveals native protein localization. Nat. Methods *9*, 480–482.

Le Gall, A., Cattoni, D.I., and Nollmann, M. (2017). Imaging of Bacterial Chromosome Organization by 3D Super-Resolution Microscopy. Methods Mol. Biol. *1624*, 253–268.

Lepore, A., Taylor, H., Landgraf, D., Okumus, B., Jaramillo-Riveri, S., McLaren, L., Bakshi, S., Paulsson, J., and Karoui, M.E. (2019). Quantification of very low-abundant proteins in bacteria using the HaloTag and epi-fluorescence microscopy. Sci Rep *9*, 1–9.

Lesterlin, C., and Duabrry, N. (2016). Investigating Bacterial Chromosome Architecture. In Chromosome Architecture, M.C. Leake, ed. (New York, NY: Springer New York), pp. 61–72.

Lesterlin, C., Ball, G., Schermelleh, L., and Sherratt, D.J. (2013). RecA bundles mediate homology pairing between distant sisters during DNA break repair. Nature *506*, 249–253.

Li, G.-W., Berg, O.G., and Elf, J. (2009). Effects of macromolecular crowding and DNA looping on gene regulation kinetics. Nature Physics *5*, 294–297.

Li, Y., Schroeder, J.W., Simmons, L.A., and Biteen, J.S. (2018). Visualizing bacterial DNA replication and repair with molecular resolution. Curr. Opin. Microbiol. *43*, 38–45.

Lindner, A.B., Madden, R., Demarez, A., Stewart, E.J., and Taddei, F. (2008). Asymmetric segregation of protein aggregates is associated with cellular aging and rejuvenation. Proc. Natl. Acad. Sci. U.S.A. *105*, 3076–3081.

Loparo, J.J., Kulczyk, A.W., Richardson, C.C., and van Oijen, A.M. (2011). Simultaneous single-molecule measurements of phage T7 replisome composition and function reveal the mechanism of polymerase exchange. Proc. Natl. Acad. Sci. U.S.A. *108*, 3584–3589.

Lutkenhaus, J. (2007). Assembly dynamics of the bacterial MinCDE system and spatial regulation of the Z ring. Annu. Rev. Biochem. *76*, 539–562.

MacDiarmid, J.A., Mugridge, N.B., Weiss, J.C., Phillips, L., Burn, A.L., Paulin, R.P., Haasdyk, J.E., Dickson, K.-A., Brahmbhatt, V.N., Pattison, S.T., et al. (2007). Bacterially derived 400 nm particles for encapsulation and cancer cell targeting of chemotherapeutics. Cancer Cell *11*, 431–445.

Manley, S., Gillette, J.M., Patterson, G.H., Shroff, H., Hess, H.F., Betzig, E., and Lippincott-Schwartz, J. (2008). High-density mapping of single-molecule trajectories with photoactivated localization microscopy. Nat. Methods *5*, 155–157.

Marklund, E., van Oosten, B., Mao, G., Amselem, E., Kipper, K., Sabantsev, A., Emmerich, A., Globisch, D., Zheng, X., Lehmann, L.C., et al. (2020). DNA surface exploration and operator bypassing during target search. Nature.

Meddows, T.R., Savory, A.P., and Lloyd, R.G. (2004). RecG helicase promotes DNA double-strand break repair. Mol. Microbiol. *52*, 119–132.

Michalet, X., and Berglund, A.J. (2012). Optimal diffusion coefficient estimation in single-particle tracking. Phys Rev E Stat Nonlin Soft Matter Phys *85*, 061916.

Mika, J.T., and Poolman, B. (2011). Macromolecule diffusion and confinement in prokaryotic cells. Curr. Opin. Biotechnol. *22*, 117–126.

Mika, J.T., Bogaart, G.V.D., Veenhoff, L., Krasnikov, V., and Poolman, B. (2010). Molecular sieving properties of the cytoplasm of Escherichia coli and consequences of osmotic stress. Molecular Microbiology *77*, 200–207.

Monteilhet, C., Perrin, A., Thierry, A., Colleaux, L., and Dujon, B. (1990). Purification and characterization of the in vitro activity of I-Sce I, a novel and highly specific endonuclease encoded by a group I intron. Nucleic Acids Res. *18*, 1407–1413.

Mullineaux, C.W., Nenninger, A., Ray, N., and Robinson, C. (2006). Diffusion of green fluorescent protein in three cell environments in Escherichia coli. J. Bacteriol. *188*, 3442–3448.

Nandakumar, J., Nair, P.A., and Shuman, S. (2007). Last stop on the road to repair: structure of E. coli DNA ligase bound to nicked DNA-adenylate. Mol. Cell *26*, 257–271.

Nenninger, A., Mastroianni, G., and Mullineaux, C.W. (2010). Size dependence of protein diffusion in the cytoplasm of Escherichia coli. J. Bacteriol. *192*, 4535–4540.

Niu, L., and Yu, J. (2008). Investigating Intracellular Dynamics of FtsZ Cytoskeleton with Photoactivation Single-Molecule Tracking. Biophys J *95*, 2009–2016.

Nolivos, S., Upton, A.L., Badrinarayanan, A., Müller, J., Zawadzka, K., Wiktor, J., Gill, A., Arciszewska, L., Nicolas, E., and Sherratt, D. (2016). MatP regulates the coordinated action of topoisomerase IV and MukBEF in chromosome segregation. Nature Communications *7*.

Nolivos, S., Cayron, J., Dedieu, A., Page, A., Delolme, F., and Lesterlin, C. (2019). Role of AcrAB-TolC multidrug efflux pump in drug-resistance acquisition by plasmid transfer. Science *364*, 778–782.

Normanno, D., Boudarène, L., Dugast-Darzacq, C., Chen, J., Richter, C., Proux, F., Bénichou, O., Voituriez, R., Darzacq, X., and Dahan, M. (2015). Probing the target search of DNA-binding proteins in mammalian cells using TetR as model searcher. Nat Commun *6*, 7357.

Parry, B.R., Surovtsev, I.V., Cabeen, M.T., O'Hern, C.S., Dufresne, E.R., and Jacobs-Wagner, C. (2014). The bacterial cytoplasm has glass-like properties and is fluidized by metabolic activity. Cell *156*, 183–194.

Ramadurai, S., Holt, A., Krasnikov, V., van den Bogaart, G., Killian, J.A., and Poolman, B. (2009). Lateral diffusion of membrane proteins. J. Am. Chem. Soc. *131*, 12650–12656.

Rampley, C.P.N., Davison, P.A., Qian, P., Preston, G.M., Hunter, C.N., Thompson, I.P., Wu, L.J., and Huang, W.E. (2017). Development of SimCells as a novel chassis for functional biosensors. Sci Rep *7*, 7261.

Raskin, D.M., and de Boer, P.A.J. (1999). Rapid pole-to-pole oscillation of a protein required for directing division to the middle of Escherichia coli. Proc Natl Acad Sci USA *96*, 4971.

Redding, S., and Greene, E.C. (2013). How do proteins locate specific targets in DNA? Chemical Physics Letters *570*.

Reece, R.J., and Maxwell, A. (1991). DNA gyrase: structure and function. Crit. Rev. Biochem. Mol. Biol. *26*, 335–375.

Reyes-Lamothe, R., Nicolas, E., and Sherratt, D.J. (2012). Chromosome replication and segregation in bacteria. Annu. Rev. Genet. *46*, 121–143.

Rhodes, J., Mazza, D., Nasmyth, K., and Uphoff, S. (2017). Scc2/Nipbl hops between chromosomal cohesin rings after loading. Elife *6*.

Ross, W., and Gourse, R.L. (2005). Sequence-independent upstream DNA-alphaCTD interactions strongly stimulate Escherichia coli RNA polymerase-lacUV5 promoter association. Proc. Natl. Acad. Sci. U.S.A. *102*, 291–296.

Rybenkov, V.V., Herrera, V., Petrushenko, Z.M., and Zhao, H. (2014). MukBEF, a chromosomal organizer. J. Mol. Microbiol. Biotechnol. *24*, 371–383.

Sanamrad, A., Persson, F., Lundius, E.G., Fange, D., Gynnå, A.H., and Elf, J. (2014). Single-particle tracking reveals that free ribosomal subunits are not excluded from the Escherichia coli nucleoid. Proc. Natl. Acad. Sci. U.S.A. *111*, 11413–11418.

Schavemaker, P.E., Śmigiel, W.M., and Poolman, B. (2017). Ribosome surface properties may impose limits on the nature of the cytoplasmic proteome. Elife *6*.

Schavemaker, P.E., Boersma, A.J., and Poolman, B. (2018). How Important Is Protein Diffusion in Prokaryotes? Front Mol Biosci *5*, 93.

Shepherd, N., Dennis, P., and Bremer, H. (2001). Cytoplasmic RNA Polymerase in Escherichia coli. Journal of Bacteriology *183*, 2527–2534.

Shuman, S. (2009). DNA Ligases: Progress and Prospects. The Journal of Biological Chemistry *284*, 17365.

Siegele, D.A., and Hu, J.C. (1997). Gene expression from plasmids containing the araBAD promoter at subsaturating inducer concentrations represents mixed populations. Proc. Natl. Acad. Sci. U.S.A. *94*, 8168–8172.

Skarstad, K., and Boye, E. (1993). Degradation of individual chromosomes in recA mutants of Escherichia coli. Journal of Bacteriology *175*, 5505.

Sliusarenko, O., Heinritz, J., Emonet, T., and Jacobs-Wagner, C. (2011). High-throughput, subpixel-precision analysis of bacterial morphogenesis and intracellular spatio-temporal dynamics. Molecular Microbiology *80*, 612.

Stracy, M., Lesterlin, C., Leon, F.G. de, Uphoff, S., Zawadzki, P., and Kapanidis, A.N. (2015). Live-cell superresolution microscopy reveals the organization of RNA polymerase in the bacterial nucleoid. PNAS *112*, E4390–E4399.

Stracy, M., Jaciuk, M., Uphoff, S., Kapanidis, A.N., Nowotny, M., Sherratt, D.J., and Zawadzki, P. (2016). Single-molecule imaging of UvrA and UvrB recruitment to DNA lesions in living Escherichia coli. Nature Communications *7*, 12568.

Stracy, M., Wollman, A.J.M., Kaja, E., Gapinski, J., Lee, J.-E., Leek, V.A., McKie, S.J., Mitchenall, L.A., Maxwell, A., Sherratt, D.J., et al. (2019). Single-molecule imaging of DNA gyrase activity in living Escherichia coli. Nucleic Acids Res *47*, 210–220.

Stylianidou, S., Kuwada, N.J., and Wiggins, P.A. (2014). Cytoplasmic Dynamics Reveals Two Modes of Nucleoid-Dependent Mobility. Biophys J *107*, 2684–2692.

Subach, F.V., Patterson, G.H., Manley, S., Gillette, J.M., Lippincott-Schwartz, J., and Verkhusha, V.V. (2009). Photoactivatable mCherry for high-resolution two-color fluorescence microscopy. Nat. Methods *6*, 153–159.

Tokunaga, M., Imamoto, N., and Sakata-Sogawa, K. (2008). Highly inclined thin illumination enables clear single-molecule imaging in cells. Nat. Methods *5*, 159–161.

Uphoff, S. (2016). Super-Resolution Microscopy and Tracking of DNA-Binding Proteins in Bacterial Cells. Methods Mol. Biol. *1431*, 221–234.

Uphoff, S., and Sherratt, D.J. (2017). Single-Molecule Analysis of Bacterial DNA Repair and Mutagenesis. Annu Rev Biophys *46*, 411–432.

Uphoff, S., Reyes-Lamothe, R., de Leon, F.G., Sherratt, D.J., and Kapanidis, A.N. (2013). Single-molecule DNA repair in live bacteria. Proceedings of the National Academy of Sciences *110*, 8063–8068.

Uphoff, S., Sherratt, D.J., and Kapanidis, A.N. (2014). Visualizing Protein-DNA Interactions in Live Bacterial Cells Using Photoactivated Single-molecule Tracking. J Vis Exp.

Uphoff, S., Lord, N.D., Okumus, B., Potvin-Trottier, L., Sherratt, D.J., and Paulsson, J. (2016). Stochastic activation of a DNA damage response causes cell-to-cell mutation rate variation. Science *351*, 1094–1097.

van der Valk, R.A., Vreede, J., Qin, L., Moolenaar, G.F., Hofmann, A., Goosen, N., and Dame, R.T. (2017). Mechanism of environmentally driven conformational changes that modulate H-NS DNA-bridging activity. Elife *6*.

Vrljic, M., Nishimura, S.Y., Brasselet, S., Moerner, W.E., and McConnell, H.M. (2002). Translational diffusion of individual class II MHC membrane proteins in cells. Biophys J *83*, 2681–2692.

Wang, X., Possoz, C., and Sherratt, D.J. (2005). Dancing around the divisome: asymmetric chromosome segregation in Escherichia coli. Genes Dev. *19*, 2367–2377.

Wegel, E., Göhler, A., Lagerholm, B.C., Wainman, A., Uphoff, S., Kaufmann, R., and Dobbie, I.M. (2016). Imaging cellular structures in super-resolution with SIM, STED and Localisation Microscopy: A practical comparison. Sci Rep *6*, 27290.

Willetts, N.S., and Clark, A.J. (1969). Characteristics of Some Multiply Recombination-Deficient Strains of Escherichia coli. Journal of Bacteriology *100*, 231.

Zandarashvili, L., Esadze, A., Vuzman, D., Kemme, C.A., Levy, Y., and Iwahara, J. (2015). Balancing between affinity and speed in target DNA search by zinc-finger proteins via modulation of dynamic conformational ensemble. Proc. Natl. Acad. Sci. U.S.A. *112*, E5142-5149.

Zawadzki, P., Stracy, M., Ginda, K., Zawadzka, K., Lesterlin, C., Kapanidis, A.N., and Sherratt, D.J. (2015). The Localization and Action of Topoisomerase IV in Escherichia coli Chromosome Segregation Is Coordinated by the SMC Complex, MukBEF. Cell Reports *13*, 2587–2596.

SUPPLEMENTARY FIGURES:

Figure S1: (A) D* histograms and model fit of PolA-PAmCherry in cells treated with methyl methanesulfonate (MMS). (B) D* histograms of PolA-PAmCherry in fixed cells, fitted with a model of immobile molecules only. (C) Scatter plot of experimentally determined D_{mobile} diffusion of 12 DNA-binding proteins against their intracellular copy number. The fitted D_{mobile} value extracted from a 2 species fit to the histograms of apparent diffusion coefficients, D*, presented in Figure 1. The copy number estimates are from literature sources are presented in Table 1. (D) Distributions histograms of apparent diffusion, D*, of three DNA-binding proteins: DNA polymerase 1 (Pol1) and RNA polymerase (RNAP) before (left) and after 60 mins treatment with 50 µg/ml rifampicin (right). Distributions are fitted with a 2-species model of immobile (in red) and mobile molecules (in blue).

Figure S2: Quantification of DNA degradation efficiency. (A) Fluorescence profiles show the distribution and intensity of DAPI signal in individual cells normalized by the cell length and sorted from left to right by increasing mean intensity. Fluorescence profile of OT / pSN1(p*P_BAD-I-SceI*) strain before (Top panel) and 120 min after I-SceI induction (lower panel) are shown. (B) Histograms of DAPI-stained DNA intracellular fluorescence in OT / pSN1(PBADI-SceI) cell population, before (blue bars) and 120 min after I-SceI induction (green bars). The percentages of cells below and above a DAPI content threshold (grey dash line) are shown. Before I-SceI induction, 17 % of cells already exhibit DNA loss likely due to the leakiness I-SceI expression from PBAD promoter. 120 min after arabinose-induced I-SceI expression, this proportion increases to 92 % of the population, with 8 % of cells still containing DNA (n= cells analyzed).

Figure S3: (A) Kymograph and concentration profiles of the fluorescence signal of MinC protein in exponentially growing *E. coli* cells. The width of the kymograph corresponds to the length L of the cell. Upon vertical splitting of the kymograph (white dashed line) and integration over space (x), the time-dependent intensity signals Fx,left(t) and Fx,right(t) are obtained. The oscillation period T2 can be

calculated by periodic fitting (blue and green lines on the left and right of the kymograph). Upon integration over time (t), a spatial concentration profile of the MinC proteins is obtained (black data points below the kymograph) and fitted (red curve). The depth D of the profile is calculated from the heights of the maxima and the minimum. (B) Oscillation of fluorescence over time in cell halves. When the time-dependent fluorescence is integrated, an almost perfect constant line is obtained (black curve). This is due to the normalization of the intensity of each pixel in respect to the total fluorescence signal at each time point. In consequence, the two periodic curves for the left and right kymograph halves are perfectly symmetric (blue and green curve). (C) Kymograph and concentration profiles of the fluorescence signal of MinC protein in filamentous cells. In filamentous cells, the time-averaged concentration profile can show more than two peaks. The distance between two peaks corresponds to half an intrinsic wavelength of the Min system. For the calculation of the oscillation period Tm in filamentous cells, the kymograph is split along the position of the minima xmin (white dashed lines in the kymograph) resulting in several stripes with a periodic pattern. Integration along x provides a periodic functions Fx,i(t) from which oscillation period Ti can be calculated. Tm represents the average for these multiple oscillation periods. (D) Kymographs of different filamentous cells show different number of oscillations. Most of them show only a single (cells 1, 4, 5 and 8) or double oscillation (cells 2, 3 and 7). In the given example one cells shows 14 peaks, which corresponds to 13 oscillations and thus 6.5 wavelengths. The respective wavelength can be then calculated from the length of the cell and the number of oscillations.

Figure S4: (A) Maintenance of protein synthesis activity upon induction of DNA degradation. Quantification of ParB-mCherry intracellular signal (a.u., arbitrary unit) produced from IPTG inducible pSN70 plasmid (P_{lac} *I-SceI*) in OT strain. I-SceI expression from pSN1 plasmid is induced by arabinose 0.2 %. Chromosome degradation alone has little impact on ParB-mCherry production. Over the course of the experiment (200 minutes), ParB-mCherry production is induced by IPTG with or without chromosome degradation. Error bars indicate the standard error and n = the numbers of cells analyzed. Two tailed P-values from Mann-Whitney non-parametric test are indicated by (n.s) non-significant P-value > 0.05, * for P-value < 0.05, ** for P-value < 0.01 and **** for P-value < 0.001. (B) Cumulative distribution plot of tracked MukB-PAmCherry trajectory step size in cells before and 120 mins after I-Scel induction. Protein diffusion remains unchanged *recA* proficient cells (*recA+*) before (magenta line) after induction (black dashed line), whereas diffusion increases after induction in *recA-* cells (blue dashed line). (C) Cumulative distribution plot of tracked Pol1-PAmCherry trajectory step size in (recA-) cells before and after I-Scel induction. Protein diffusion increases with I-Scel induction time from 0 to 90 mins, but increases only modestly beyond 90 mins induction.

Figure S5: A fraction of cells did not undergo full DNA degradation and these cells showed little change in the diffusion profiles. (A) Fluorescence image of SytoGreen stained DNA in cells after 120 mins of I-SceI induction showing DNA+ and DNA-free cells (top). The brightfield image of the same cells overlaid with the categorized trajectories of RNAP-PAmCherry tracks with immobile molecules in red and mobile molecules in blue (bottom). The lower-right insert presents a zoom of one DNA+ and one DNA-free cell. (B) Cumulative distribution of LacI-PAmCherry trajectory displacement steps in cells having high (DNA+ cells in blue) or low (DNA-free cells in red) SytoGreen fluorescence compared to the unperturbed cells (in black).

Figure S6: D^* distribution (grey bars) of MukB-PAmCherry, Pol1-PAmCherry, LigA-PAmCherry and LacI-PAmCherry in DNA-free cells 120 min after I-SceI induction measured with an exposure time of 15 ms (left) and 5 ms (right). The D^* distribution generated from simulated molecule trajectories with the same diffusion coefficient, D_{free}, at 15 ms (left) and 5 ms (right) exposure times.

Figure 1

Figure 2

A

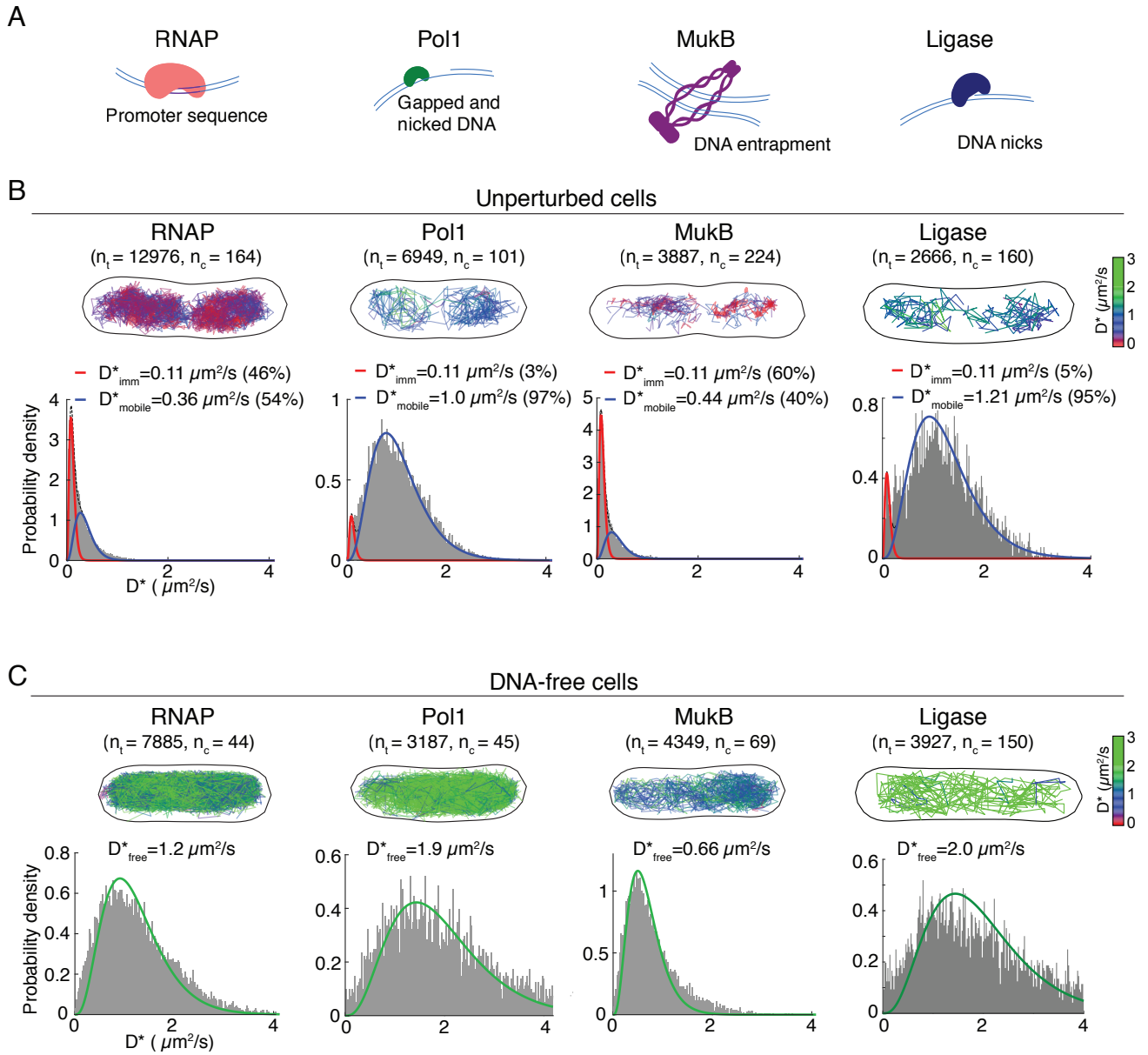B

time after I-SceI induction (min)

C

D

E

F

G
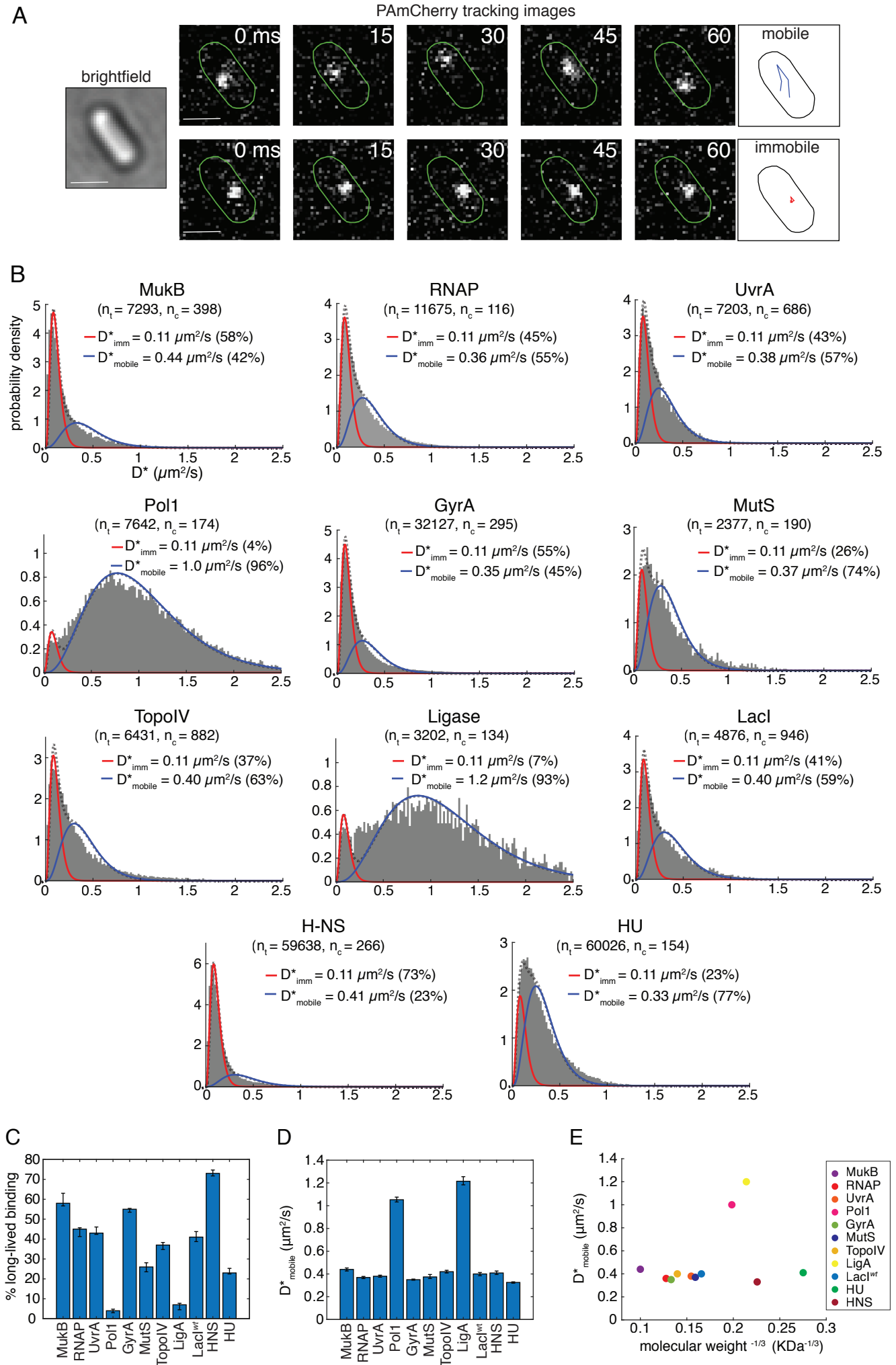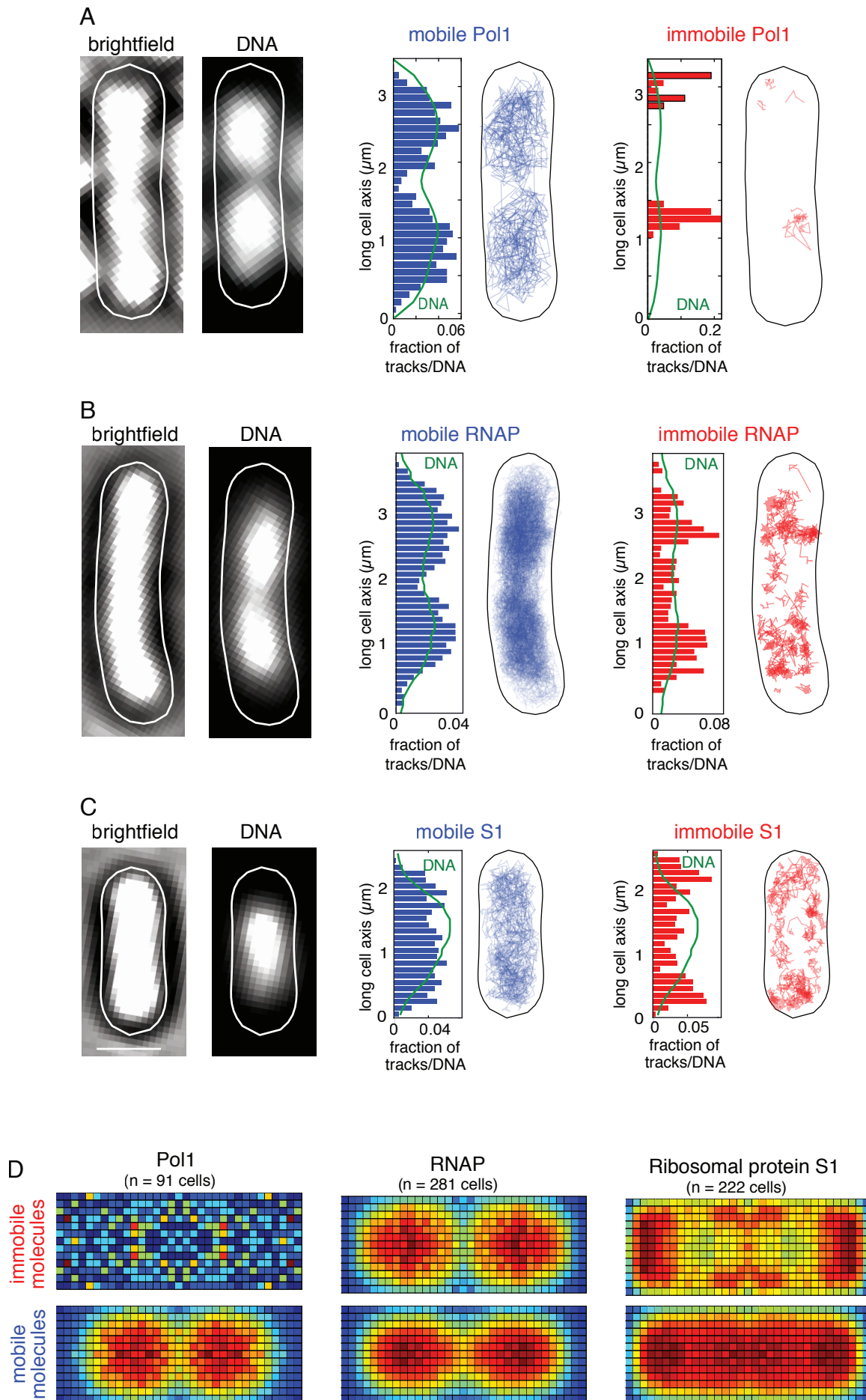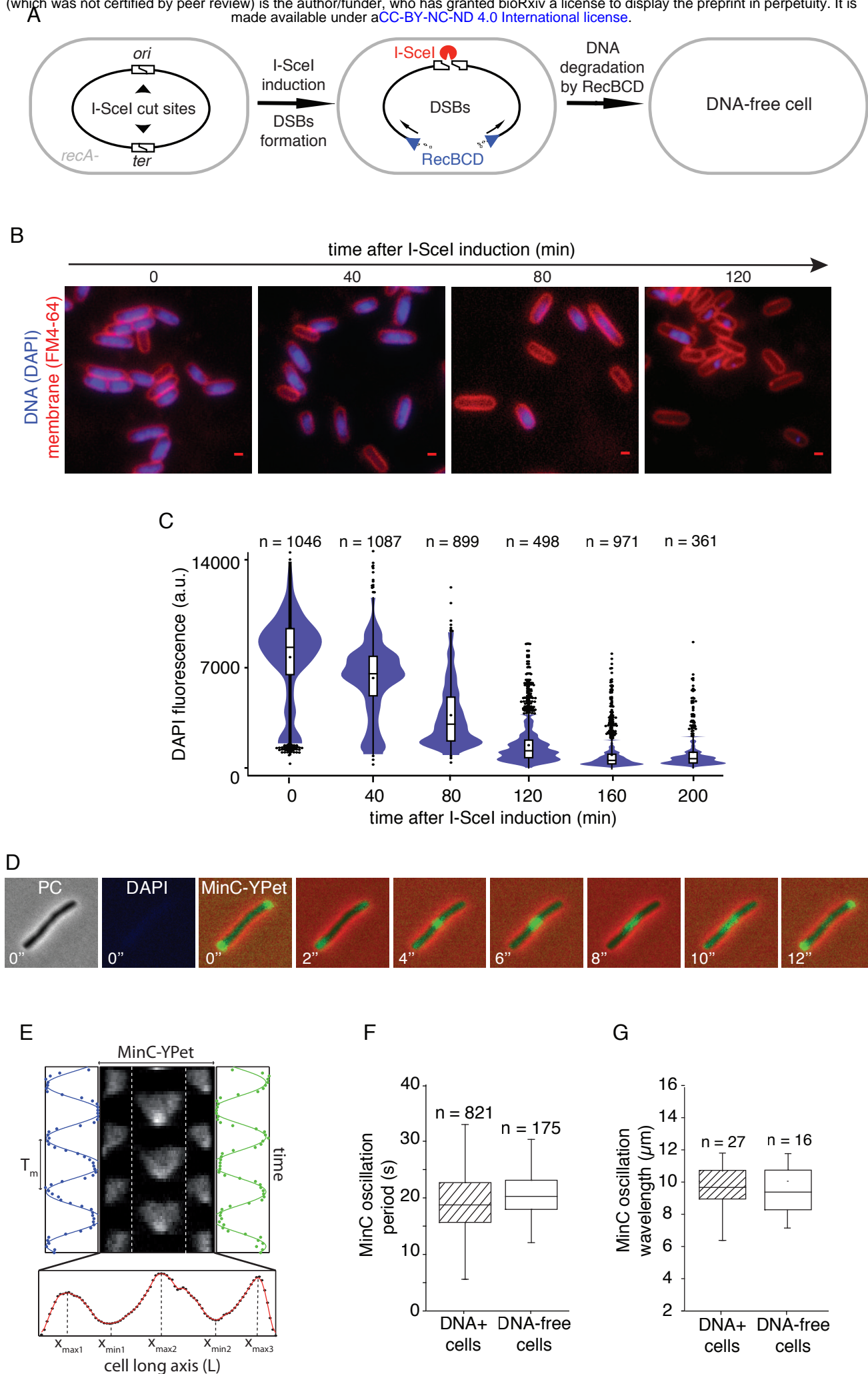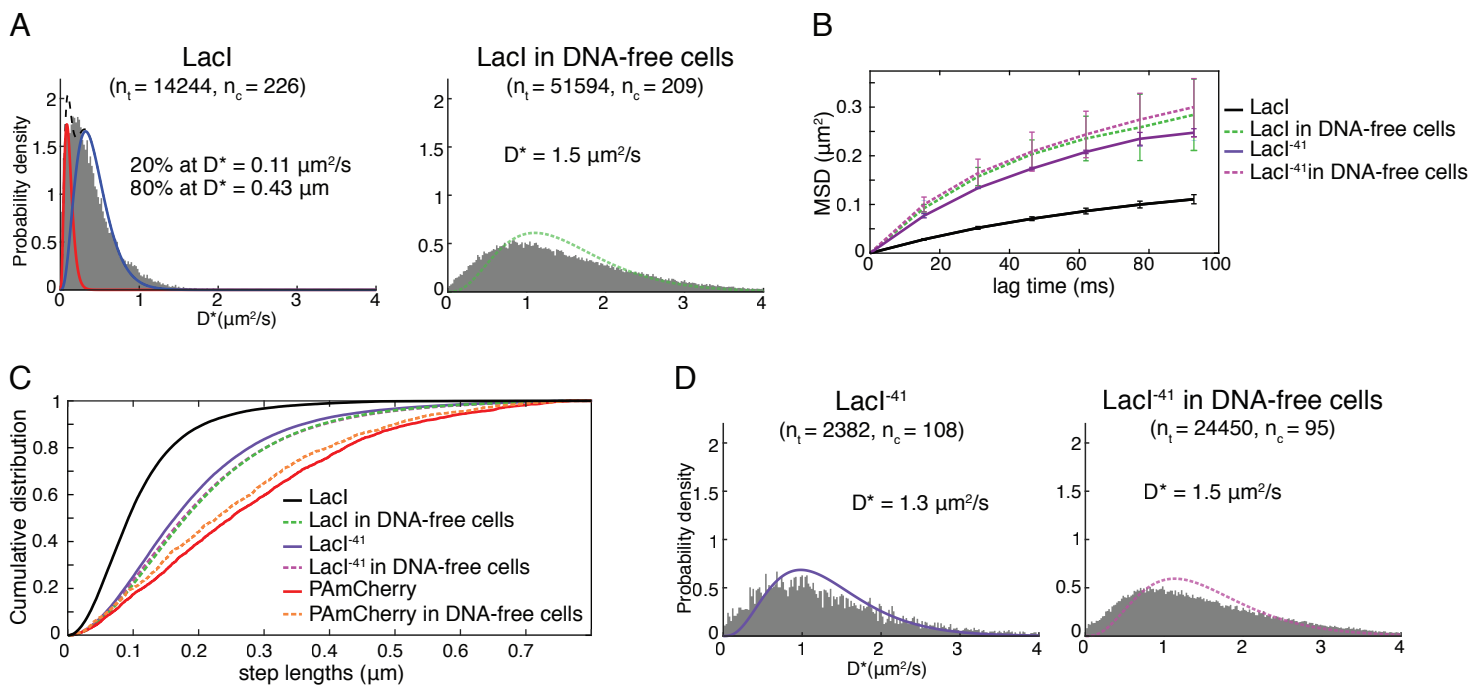
Figure 3

Figure 4

Figure 5

Figure 6

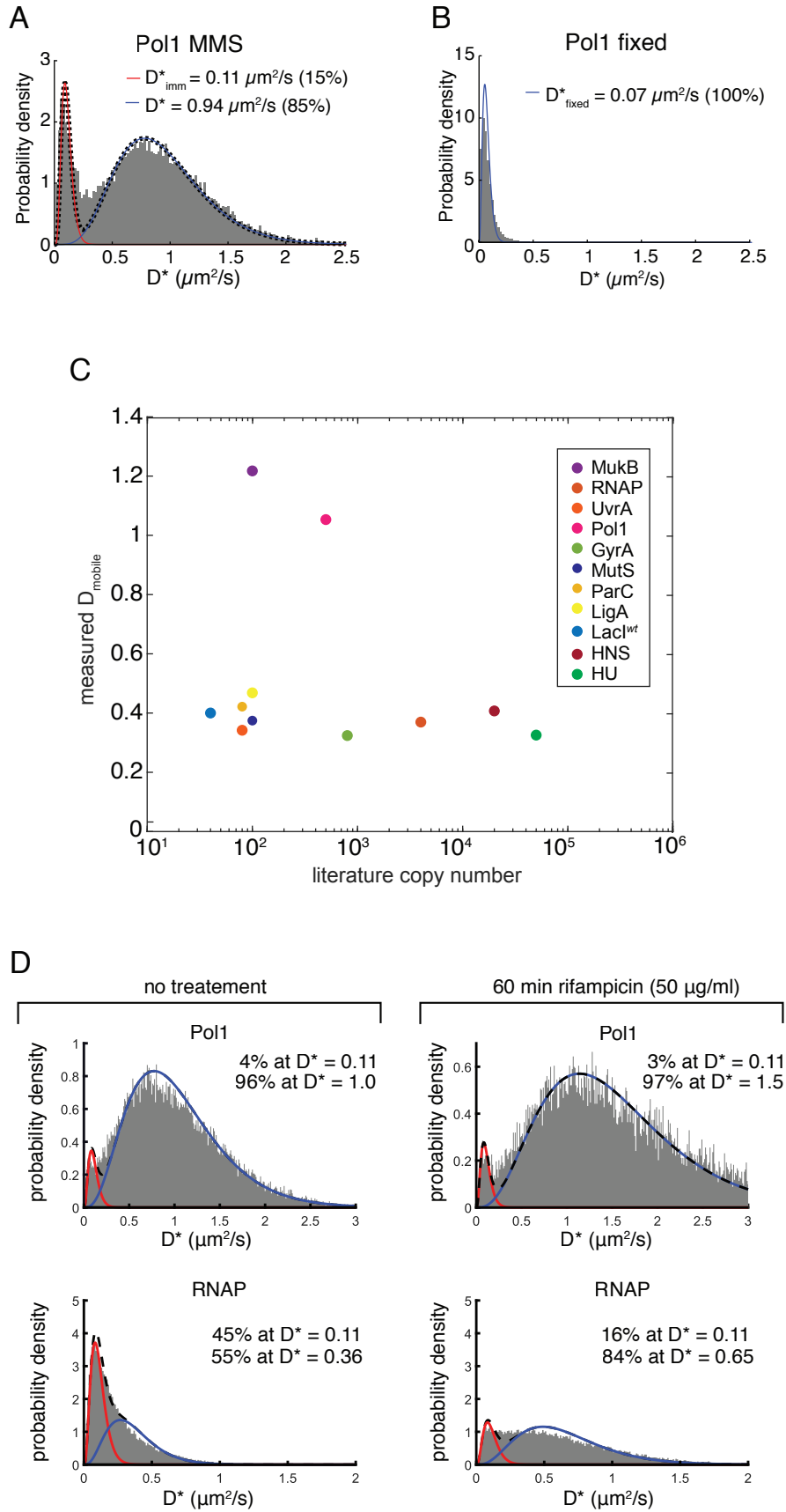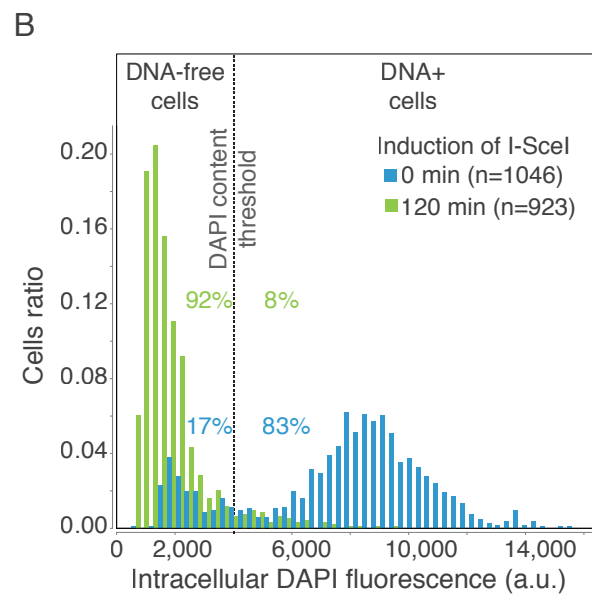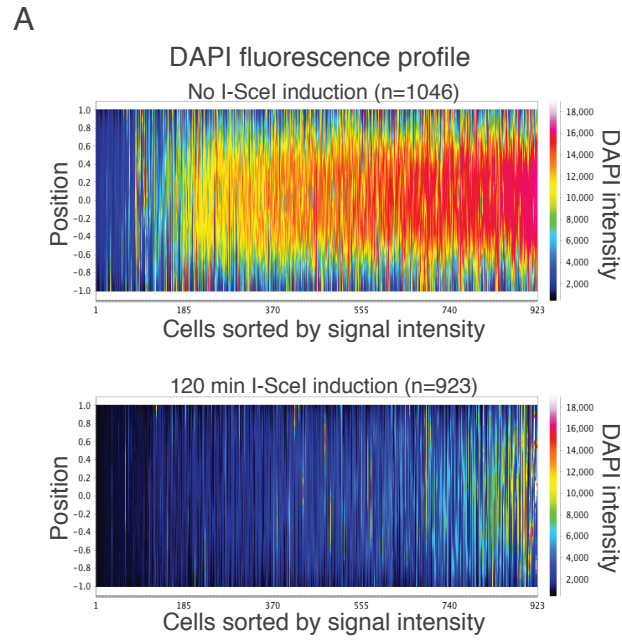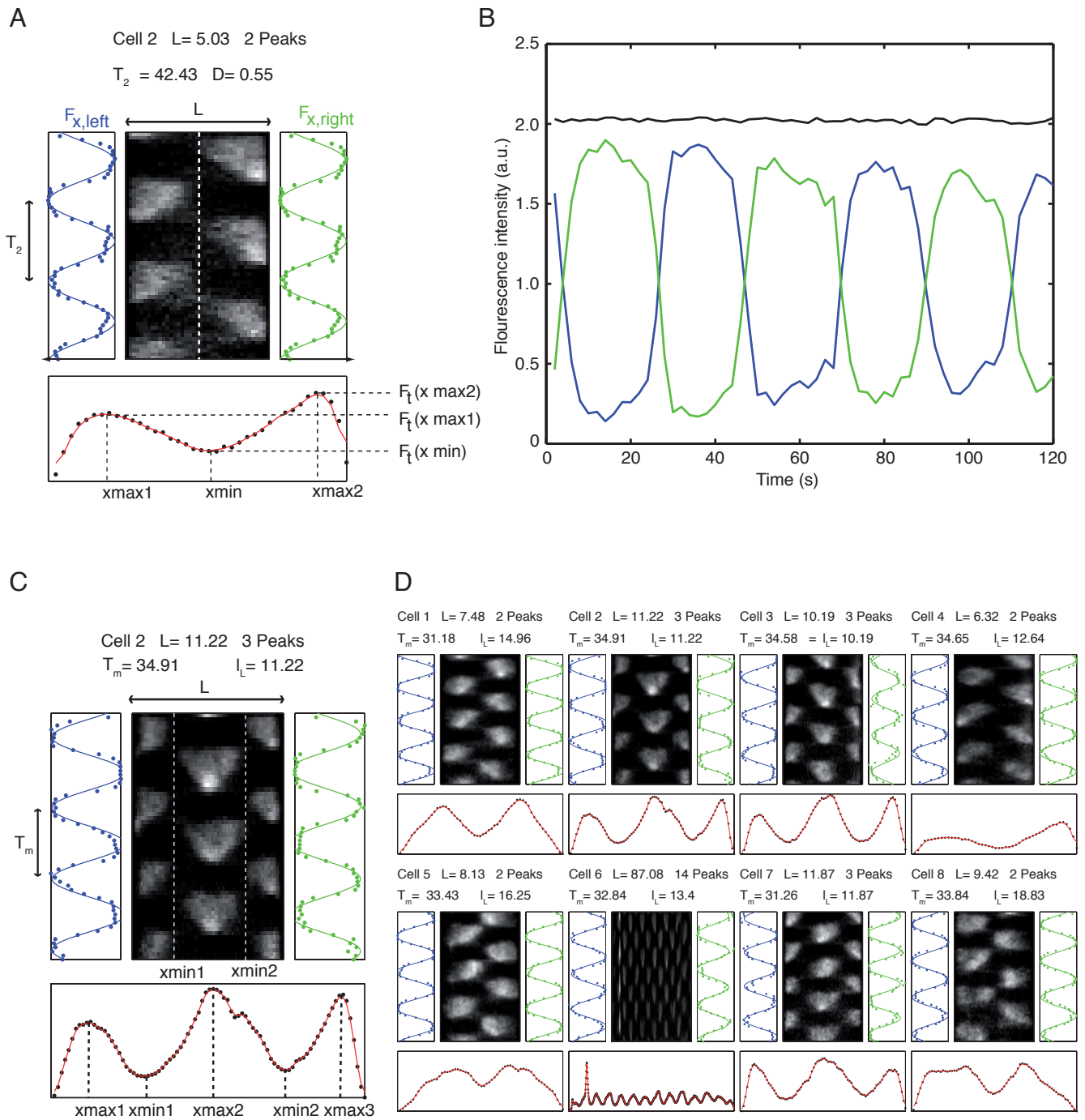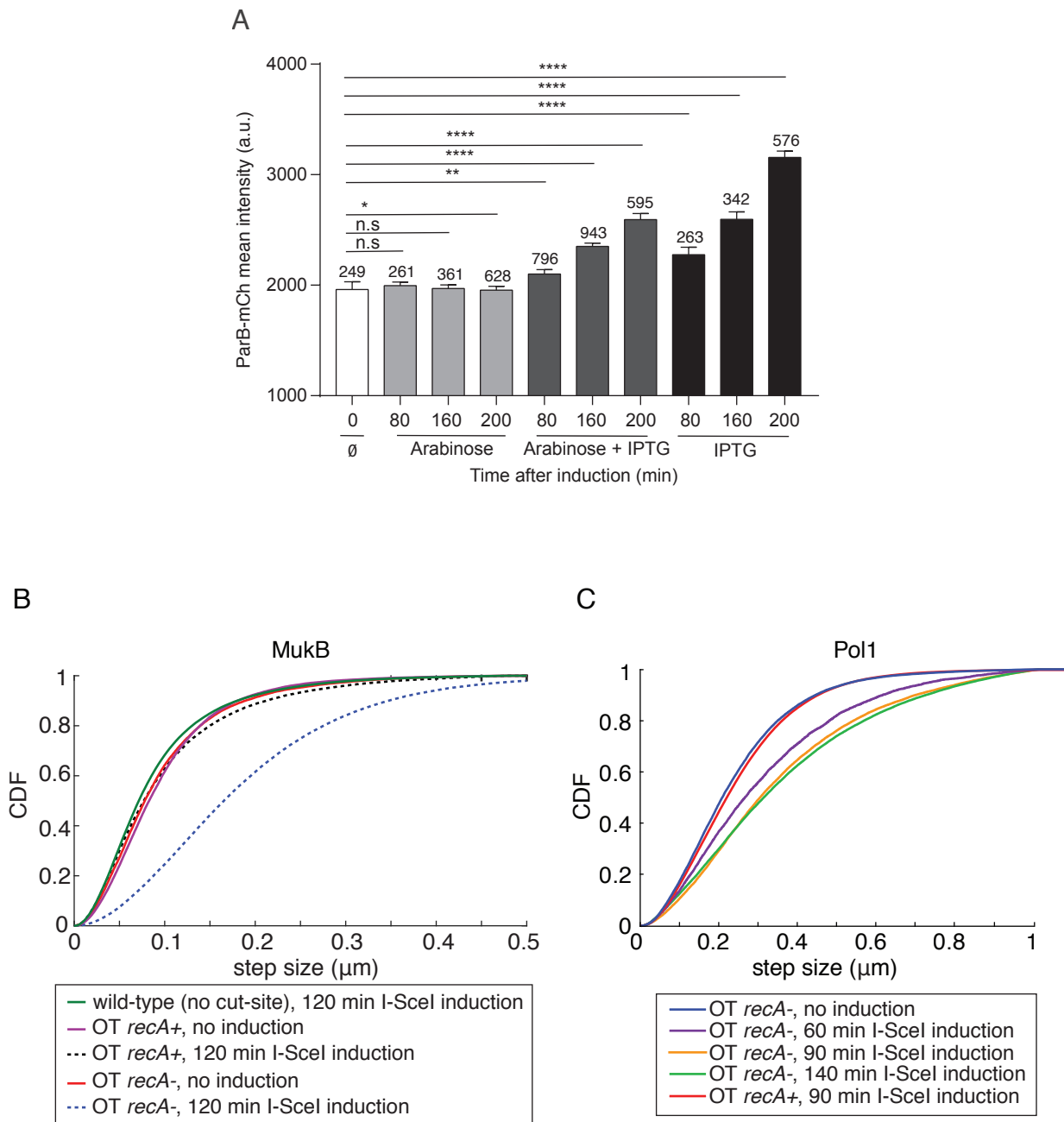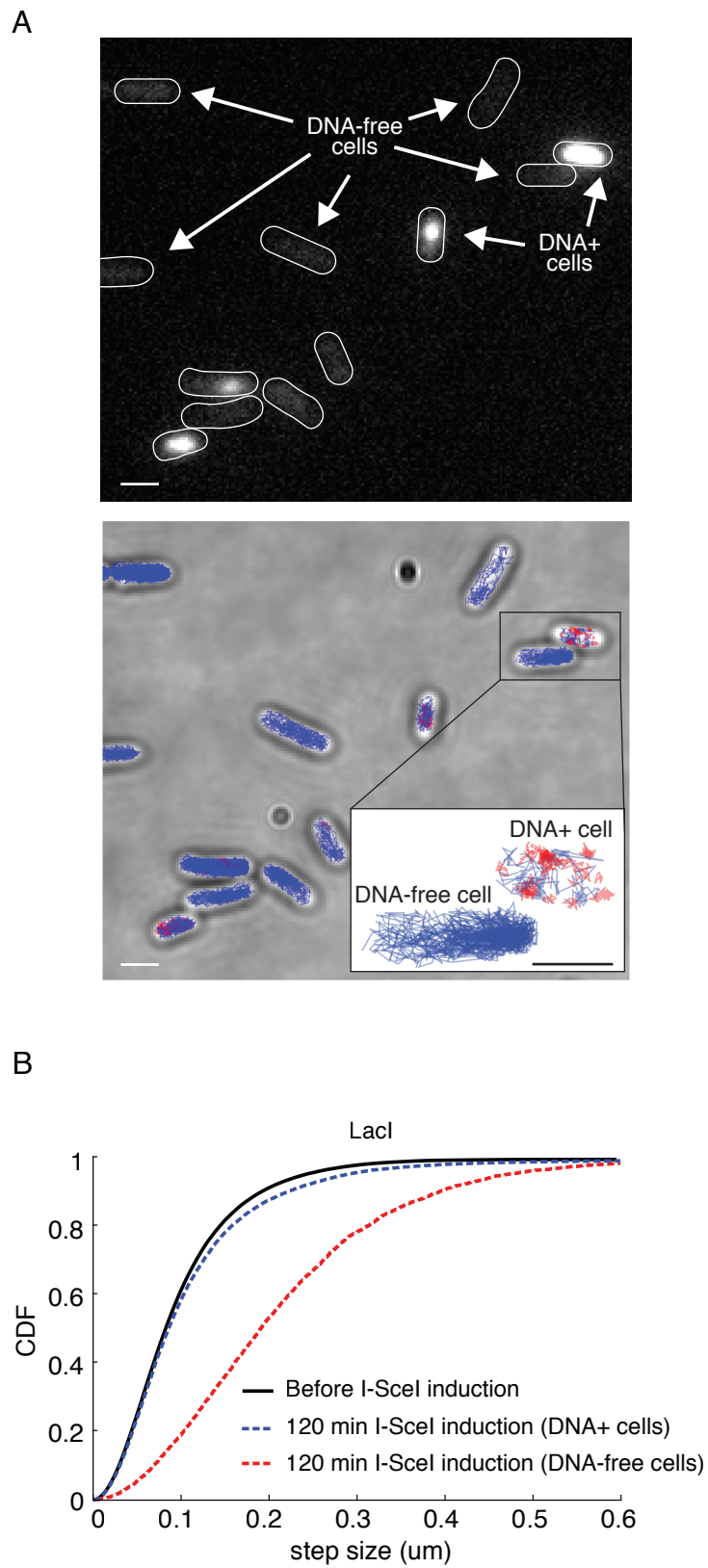Figure S1

A

B

Fig. S2

Fig. S3

Fig. S4

A

B
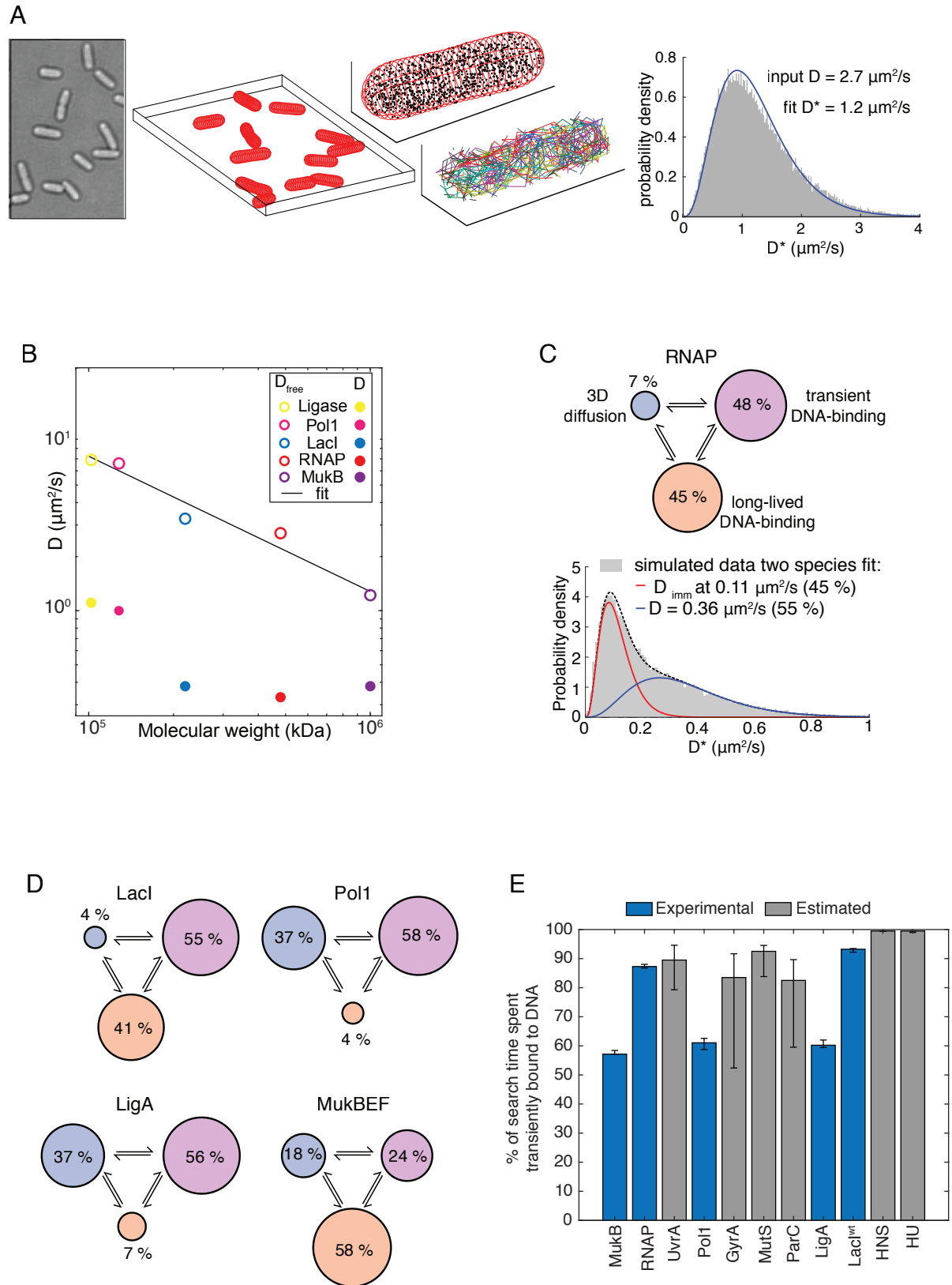
Fig. S5
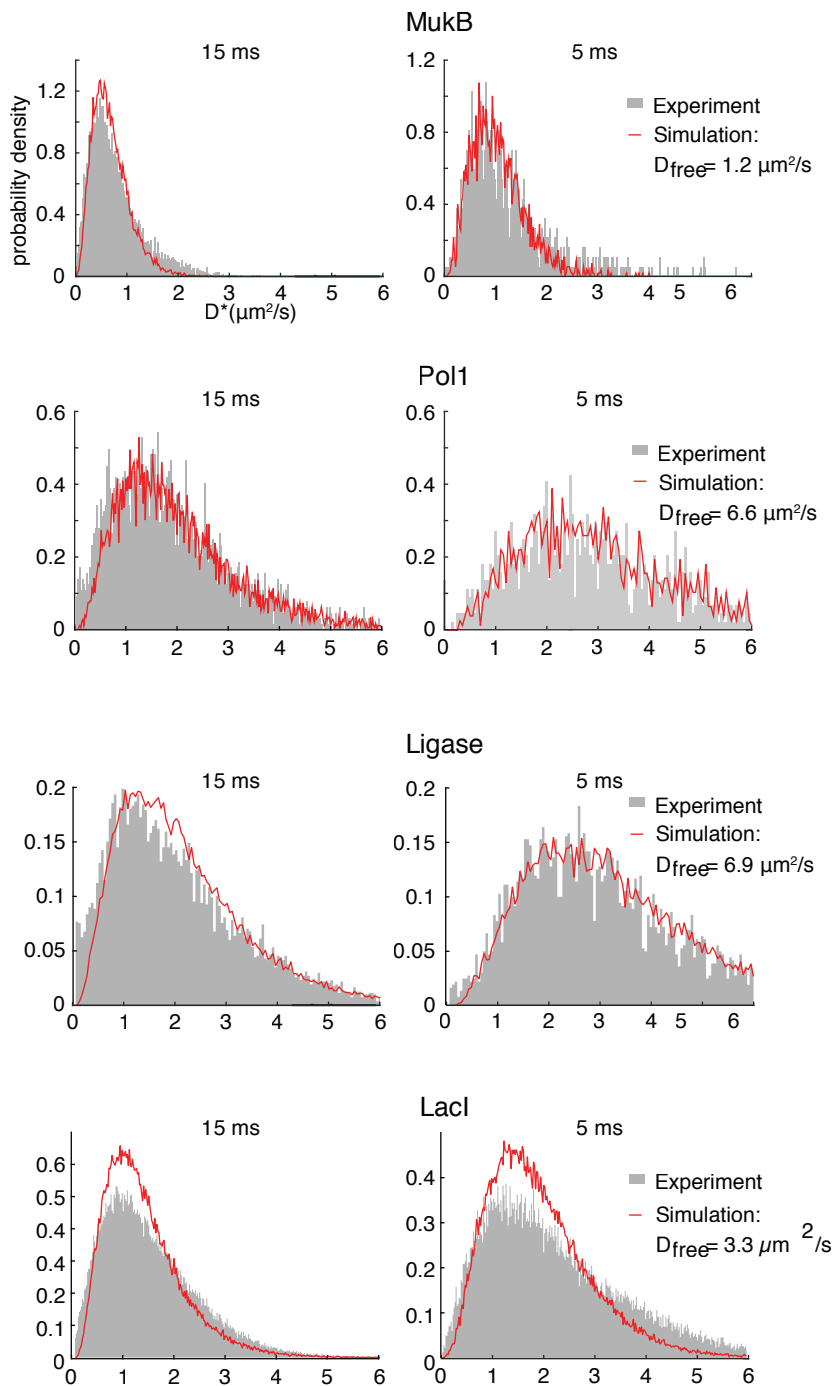
Fig. S6

Table S1 **Strains and plasmids used in this study**

Strain	Relevant Genotype	Source or Reference
MG1655	F- lambda- *ilvG*- *rfb*-50 *rph*-1	CGSC#: 7740
TB28	MG1655 *ΔlacIZYA*	Bernhardt and de Boer, 2005
TB28 I-SceI^{CS}-ilvA	TB28 *I-SceI^{CS}-ilvA-FRT* (3953 kb)	TB28 × P1.*I-SceI^{CS}-ilvA* to Cm^r, *cat* removed via pCP20
TB28 *I-SceI^{CS}-ydeO*	TB28 *I-SceI^{CS}-ydeO-FRT-cat-FRT* (1580 kb)	TB28 × P1. *I-SceI^{CS}-ydeO* to Cm^{r,}
OT	TB28 *I-SceI^{CS}-ilvA-FRT, I-SceI^{CS}-ydeO-FRT*	TB28 *I-SceI^{CS}-ilvA* × P1.*I-SceI^{CS}-ydeO* to Cm^r, *cat* removed via pCP20
RNAP-PAmCherry	MG1655 *rpoC-PAmCherry-FRT-kan-FRT*	Stracy et al., 2015
HU-PAmCherry	MG1655 *hupB-PAmCherry-FRT-kan-FRT*	Stracy et al., 2015
HN-S-PAmCherry	MG1655 *Hns-PAmCherry-FRT-kan-FRT*	Stracy et al., 2015
FIS-PAmCherry	MG1655 *fis-PAmCherry-FRT-kan-FRT*	Uphoff et al., 2013
LacI-mCherry	MG1655 *LacI-PAmCherry*	Garza de Leon et al., 2017
Pol1-PAmCherry	MG1655 *polA-PAmCherry-FRT-kan-FRT*	Uphoff et al., 2013
LigA-PAmCherry	MG1655 *ligA-PAmCherry-FRT-kan-FRT*	Uphoff et al., 2013
UvrA-PAmCherry	MG1655 *uvrA-PAmCherry-FRT-kan-FRT*	Stracy et al., 2016
MutS-PAmCherry	MG1655 *mutS-PAmCherry-FRT-kan-FRT*	Uphoff et al., 2016
TopoIV-PAmCherry	MG1655 *parC-PAmCherry-FRT-kan-FRT*	Zawadzki et al., 2015
MukB-PAmCherry	MG1655 *mukB-PAmCherry-FRT-kan-FRT*	Badrinarayanan et al., 2012
GyrA-PAmCherry	MG1655 *gyrA-PAmCherry-FRT-kan-FRT*	Stracy et al., 2019
recA- strain	TB28 *recAT233C-Tet*	Lesterlin et al., 2014
MinC-Ypet	*minC-Ypet*	Bisicchia et al., 2013
OT RNAP-PAmCherry	OT *rpoC-PAmCherry-FRT-kan-FRT*	OT x P1. RNAP-PAmCherry to Km^r
OT Pol1-PAmCherry	OT *polA-PAmCherry-FRT-kan-FRT*	OT x P1. Pol1-PAmCherry to Km^r
OT LigA-PAmCherry	OT *ligA-PAmCherry-FRT-kan-FRT*	OT x P1. LigA-PAmCherry to Km^r
OT MukB-PAmCherry	OT *mukB-PAmCherry-FRT-kan-FRT*	OT x P1. MukB-PAmCherry to Km^r
OT LacI-PAmCherry	OT */ p lacI-PAmCherry*	Transformation of p *lacI-PAmCherry* into OT strain
OT LacI[41]-PAmCherry	OT */ p lacI^{41}-PAmCherry*	Transformation of p *lacI^{41}-PAmCherry* into OT strain
OT Free PAmCherry	OT pBAD\HisB PAmCherry1	Transformation of pBAD\HisB PAmCherry1into OT strain
OT FIS-PAmCherry	OT *fis-PAmCherry-FRT-kan-FRT*	OT x P1. FIS-PAmCherry to Km^r
OT *recA-*	OT *recAT233C-Tet*	OT x P1. *recAT233C-Tet* to

		Tc
OT RNAP-PAmCherry *recA-*	OT *rpoC-PAmCherry-FRT-kan-FRT*	OT RNAP-PAmCherry x P1. *recAT233C-Tet* to Tc
OT Pol1-PAmCherry *recA-*	OT *polA-PAmCherry-FRT-kan-FRT*	OT Pol1-PAmCherry x P1. *recAT233C-Tet* to Tc
OT LigA-PAmCherry *recA-*	OT *ligA-PAmCherry-FRT-kan-FRT*	OT LigA-PAmCherry x P1. *recAT233C-Tet* to Tc
OT MukB-PAmCherry *recA-*	OT *mukB-PAmCherry-FRT-kan-FRT*	OT MukB-PAmCherry x P1. *recAT233C-Tet* to Tc to Km[r]
OT LacI-PAmCherry *recA-*	OT */ P lacI-PAmCherry*	Transformation of *P lacI-PAmCherry* into OT *recA-*
OT LacI[41]-PAmCherry *recA-*	OT */ P lacI[41]-PAmCherry*	Transformation of *P lacI[41]-PAmCherry* into OT *recA-*
OT Free PA-mCherry *recA-*	OT pBAD\HisB PAmCherry1	Transformation of pBAD\HisB PAmCherry1 into OT *recA-* strain
Plasmids		
p *lacI-PAmCherry*	LacI-PAmCherry producing plasmid	Garza de Leon et al., 2017
p *lacI[41]-PAmCherry*	LacI[41]-PAmCherry producing plasmid	Garza de Leon et al., 2017
pBAD\HisB PAmCherry1	PAmCherry1 producing plasmid	Endesfelder et al., 2013
pCP20	Flp expression plasmid	Datsenko et al., 2000
p*ParBmCherry* (pSN70)	IPTG inducible expression of N-terminal fusion mCherry-ParB$_{PMT1}$	Nolivos et al., 2019
pI-SceI (pSN1)	Arabinose inducible expression of I-SceI endonuclease	Gift from Sophie Nolivos